Error analysis of a conceptual cloud doppler stereoradar with polarization diversity for better understanding space applications

# Error Analysis of a Conceptual Cloud Doppler Stereoradar with Polarization Diversity for Better Understanding Space Applications

ALESSANDRO BATTAGLIA

*Department of Physics and Astronomy, University of Leicester, Leicester, United Kingdom*

PAVLOS KOLLIAS

*Department of Atmospheric and Oceanic Sciences, McGill University, Montreal, Canada*

(Manuscript received 14 January 2014, in final form 2 April 2015)

ABSTRACT

An error budget analysis is performed for retrieval of along-track winds based on the design of a spaceborne Doppler radar using polarization diversity. The analysis is conducted within the framework of a case study of an Atlantic hurricane. The proposed concept consists of either a Ka-band or W-band stereoradar mounted on an LEO satellite equipped with both nadir- and forward-viewing beams and with an optional cross-scanning capability. Such a radar design is intended for observing the microphysical and dynamical structures of cloud systems, including disturbed mesoscale convective systems. Because of the high winds involved in such weather phenomena and because of the Doppler fading introduced by platform motion, polarization diversity is adopted. The simulation framework enables a breakdown of the Doppler velocity measurement error budget into its most important components, that is, nonuniform beamfilling, multiple scattering, and inherent signal noise. The impact of each of these error terms on the total error depends on the adopted integration length, the number of scanned tracks, and the specifics of the radar. This allows for optimally selecting an integration length suitable for minimizing the total rms velocity error. The analysis shows that the use of a large antenna could achieve impressive measurement accuracy of the along-line-of-sight wind velocities. Notably, this would be the case for integration lengths longer than 3 km, even when carrying out cross-track scanning for up to 17 separate tracks. Examples of retrieved along-track wind fields also reveal that the large antenna configurations are capable of identifying and quantifying the foremost dynamic features (e.g., vertical wind shear and convergence/divergence regions).

## 1. Introduction

Current operational spaceborne radars offer global-scale coverage and have been able to probe the vertical structure of clouds and precipitation by making measurements of incoherent radar reflectivity quantities at various millimeter-region wavelengths (see Kummerow et al. 1998; Stephens et al. 2002; Hou et al. 2014). Going beyond this type of measurement, the coming availability of coherent radar Doppler velocity measurements from space will significantly improve the classification of cloud and precipitation genres, reduce the uncertainty in quantitative retrievals of in-cloud winds and hydrometeor properties, and ultimately lead to new understanding and insights concerning cloud dynamics and hydrometeor lifetimes/sedimentation rates (see Battaglia et al. 2011; Sy et al. 2013; Kollias et al. 2014). Currently, the only planned mission designed to obtain Doppler measurements from space is the joint European Space Agency (ESA)–Japan Aerospace Exploration Agency (JAXA) Earth Clouds, Aerosols and Radiation Explorer (EarthCARE) mission (see Illingworth et al. 2015). The EarthCARE satellite is due to launch in 2017 and will deploy the first spaceborne Doppler radar at W band (94 GHz), noting that the Doppler measurements will be restricted to nadir view only. Whereas it is undeniable that, once operational, EarthCARE will provide valuable insights into the challenge of making millimeter-wave Doppler measurements from space and will reveal exciting new information concerning clouds and precipitation, it should be considered as the first step toward more comprehensive

*Corresponding author address:* Alessandro Battaglia, Department of Physics and Astronomy, University of Leicester, University Road, Leicester LE1 7RH, United Kingdom.
E-mail: ab474@le.ac.uk

DOI: 10.1175/JTECH-D-14-00015.1

missions. Eventually, the advanced missions will provide more accurate Doppler measurements over wide swaths of the atmosphere using both nadir and off-nadir views and will likely employ multifrequency radar instruments equipped with polarization diversity to enhance retrieval opportunities and beat down uncertainties in the underlying retrieval parameters.

High-frequency Doppler radars with scanning capabilities have the potential to observe simultaneously the three-dimensional kinematic and microphysical states of mesoscale weather systems and extreme weather events, such as tropical storms and cyclones, intense convection, and large hail events. This measurement approach has already been applied successfully using ground-based Doppler observations of supercells with centimeter-wave radars (Yuter and Houze 1995) and finer-scale phenomena, such as dryline frontal zones and tornado vortices with millimeter-wave radars (e.g., Bluestein et al. 2004). Similarly, airborne systems have provided a unique view of the vertical structures of hurricanes and squall lines (e.g., Heymsfield et al. 1996, 1999, 2001). From space, the potential value of a scanning Doppler radar instrument may be best portended by examining existing W-band radar reflectivity images acquired by *CloudSat* satellite (see Stephens et al. 2008) and imagining possible improvements to the observational framework. An overpass over the eye of Hurricane Bill churning in the Atlantic on 19 August 2009 is shown in Fig. 1. At the overpass time, Hurricane Bill strengthened to a category 4 storm while completing an eyewall replacement cycle. The eye is completely cirrus free with intense reflectivities (red) surrounding the eyewall, while the upper edges of the eyewall are tilted toward the south. Even if some areas are clearly affected by total attenuation (e.g., the region close to 20° latitude), and likely by multiple scattering, there is an abundance of detected clouds that reveal certain attributes of the internal structure of the hurricane, especially above the freezing level. The region located above the white line [which is identified according to a cumulated reflectivity constraint proposed in Battaglia et al. (2011)] can safely be assumed to be multiple scattering free, and as such it is a source of range-resolved information for the system under observation. Thanks to its polarization capability, the system proposed in this study is actually capable of properly identifying the regions corrupted by multiple scattering and filtering them out. This clearly demonstrates the potential of millimeter-wave radars even when observing such extreme systems. A complete picture of the system can only be obtained in a multifrequency approach with the inclusion of observations at X or Ku band.

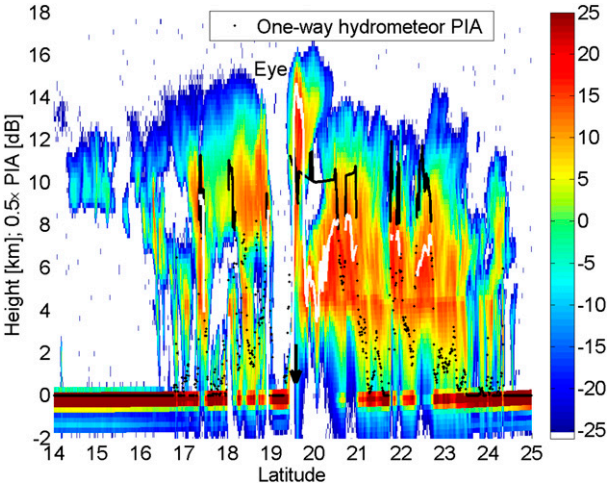


FIG. 1. *CloudSat* radar vertical reflectivity profile at W band for overpass of Atlantic Hurricane Bill on 19 Aug 2009 between 1722 and 1725 UTC (corresponding to along-track distance of 1300 km) acquired from *CloudSat* satellite data. Estimated hydrometeor-induced one-way path-integrated attenuations [produced by the *CloudSat* t(2C-PRECIP-COLUMN algorithm described by Mitrescu et al. (2010)] are shown with black dots. Where dots are united with a continuous line, the corresponding profiles are likely affected by significant multiple scattering according to the path-integrated thresholding discussed in Battaglia et al. (2008). For such profiles the white line indicates the level below which single-scattering approximation is likely to fail according to the criterion proposed in Battaglia et al. (2011).

Currently, there is great interest in quantifying the errors associated with Doppler measurements from space, not only in the context of the EarthCARE mission, but also for preparing future spaceborne Doppler radar missions with scanning capabilities. The main objective of this study is a component-by-component error analysis of retrieving along-track wind velocities in cloud media using different configurations of a millimeter-wave scanning Doppler stereoradar with polarization diversity conceived for a space platform in low-Earth orbit (LEO). A considerable number of cross-track Doppler measurements are included to ensure extended sampling and coverage. The error analysis is conducted using a state-of-the art spaceborne radar forward radiation model in combination with the Weather Research and Forecasting (WRF) Model (described by Skamarock and Klemp 2008) to simulate an Atlantic hurricane at 1-km resolution accompanied by associated simulated radar observations. This enables representing a wide range of convective and stratiform cloud conditions in part with embedded precipitation at varying degrees of rain-rate intensity.

Such observations are not currently available from space. It is now well accepted that their availability could provide valuable information for a variety of

scientific communities, including those involved with cloud research, tropical storm/cyclone research, and operational weather prediction. These communities have different requirements insofar as spatial–temporal coverages and radial Doppler velocity uncertainties. Spatial–temporal coverage requirements of the prospective user community are not discussed here and, as is typical in the case of using LEO satellites for operational applications, temporal coverage can be addressed by using a constellation of satellites. Here, the focus is directed toward the uncertainty in the measurement of the radial Doppler velocity component in order to better understand the likely performance of a spaceborne millimeter-wave Doppler stereoradar instrument. The assimilation of Doppler velocities has already granted promising results, as noted in the studies of, for example, Gao et al. (1999) and Snyder and Zhang (2003). Although limited only to areas with hydrometeors, Doppler radar measurements are directly related to the three components of the wind vector by straightforward geometrical manipulations. As shown in Zhang et al. (2009), wind speed accuracies on the order of only $3\,m\,s^{-1}$ can lead to significant weather prediction improvements when used for data assimilation. Notably, the proposed stereoradar concept has great potential for characterizing the scales and/or organization of observed cloud systems, factors that have important implications for improving cloud and prediction models in general. Thus, Doppler radar measurements from space are valuable for 1) improving quantitative estimates of hydrometeor properties (especially mass, size, and shape factors), 2) characterizing in-cloud internal dynamics by the capture of Doppler velocities, and 3) understanding the organization and controlling dynamics of intensifying and decaying mesoscale cloud systems. It is important to recognize that at nadir view, Doppler velocity accuracies of order $1\,m\,s^{-1}$ are sufficient to reasonably determine the intensity of convection (ESA 2006; Tanelli et al. 2010), whereas more stringent accuracies on the order of $0.2\,m\,s^{-1}$ are needed to carry out useful quantitative hydrometeor retrievals involving mass-size factors (Joe et al. 2010). When cross-track scanning out of the nadir-view configuration, Doppler velocities with accuracies of better than $2\,m\,s^{-1}$ and spatial resolutions of no more than 10 km are required for adequate estimates of the horizontal wind field (Eyre et al. 2002; Stoffelen et al. 2006). We emphasize that, ultimately, it is the objective of this investigation and follow-on investigations to determine to what extent these requirements could be met by a millimeter-band scanning Doppler stereoradar (possibly using multiple frequencies, each equipped with polarization separation capability) mounted on a LEO satellite platform(s).

The paper is organized as follows: section 1 provides an introduction, while section 2 revisits the background for the Doppler stereoradar concept, including presentation of details concerning the technical specifications relevant to such an instrument. Section 3 discusses the modeling framework, including salient results for the case study of a simulated Atlantic hurricane. Section 4 presents a comprehensive analysis of the various error sources associated with the radar observations, whereas Section 5 illustrates examples of retrieved along-track winds, including discussion of the corresponding error budget. Finally, section 6 draws the major conclusions and recommendations for future research.

## 2. Stereoradar concept

Stereoradar meteorology was first broached for satellite applications by Testud and Amayenc (1989) as a promising technique to observe precipitation. The underlying idea is that the observation of the same reflecting volume (with time lags on the order of 1 min) from two different viewing directions significantly helps in recovering the attenuation field, which under appropriate assumptions is better related to precipitation than the radar reflectivity field itself. To have accurate estimates in light and moderate rain and to reduce the impact of drop size distribution variability and nonuniform beamfilling (NUBF) effects, frequencies in the K and Ka bands were recommended (Testud et al. 1992). Amayenc et al. (1993) further investigated the possibility of adding Doppler capabilities for a dual-view 24-GHz system with a 5.4-m-diameter antenna and concluded that the Doppler option could greatly increase the instrument's scientific potential by providing the along-track component of horizontal wind and a near-vertical component of Doppler velocity. Today, some 20 years since these earlier studies and with the experience gained from airborne measurements based on multifrequency, multiangle Doppler radar systems (e.g., Heymsfield et al. 1996; Guimond et al. 2014) as well as from three ongoing radar-equipped satellite missions—the Tropical Rainfall Measuring Mission (TRMM) using a Ku-band radar and launched on 27 November 1997 from Tanegashima Space Center (TSC), Japan (see Simpson et al. 1996; Kummerow et al. 1998); the *CloudSat* mission using a W-band radar and launched on 28 April 2006 from Vandenberg Air Force Base, California (see Stephens et al. 2002, 2008); and the Global Precipitation Measuring (GPM) mission using a dual Ku-/Ka-band radar and launched on 27 February 2014 from TSC (see Smith et al. 2007; Hou et al. 2014)—it is worth reconsidering the potential of a Doppler stereoradar for future space applications.

Herein we assume a particular stereoradar system that uses a nadir-direction and forward-direction dual-viewing configuration but with the additional capability to cross-track scan from either configuration, as shown schematically in Fig. 2. Note in this diagram that $\alpha$ is the angular separation between the nadir-view and forward-view configurations, $\theta$ is the half angle of the nadir-view configuration cross-track scan domain, while $H_{\rm sat}$ and $V_{\rm sat}$ represent the height and on-orbit velocity of the satellite platform, respectively. Although the antenna design is beyond the scope of this paper, ideally an electronically scanning antenna similar to those used on the TRMM and GPM satellites and of comparable or larger size would be required. Dual-polarimetric capabilities on phased-array antennas even at W band (as required by our proposed design) are emerging technologies currently under development (see Bluestein et al. 2014).

As Fig. 2 indicates, the selection of viewing directions facilitates obtaining both a detailed depiction of in-cloud wind velocities and a representation of vertical dynamics and microphysics of the cloud system under observation. In its minimal option, the proposed instrument would only sample along track at the two different viewing angles. (Note that this could also be achieved by employing a convoy of two satellites, one nadir viewing and the other forward viewing using simpler dish antennas, thus avoiding the extra expense of the electronic scanning antennas. This would also eliminate the temporal mismatch between the two measuring views, demanded by the use of a single platform, but by the same token, savings from use of simpler antennas would be offset, perhaps to a greater degree, because two separate satellite systems would be involved.) Cross-track scanning over the satellite trajectory makes feasible sampling at discrete incidence angle $\theta_j$ with $j = 1, \ldots, N_T$, where $N_T$ is the number of tracks (i.e., beam positions along a cross-track scan) as depicted in Fig. 2. In such a configuration the same approximate atmospheric volume can be probed within a short time interval $\Delta t$, where $\Delta t \approx H_{\rm sat}\tan(\alpha)/V_{\rm sat}$ and is on the order of 1 min (indicated by positions A and B in Fig. 2). This results in the measurement of two independent radial velocities, $V_1$ and $V_2$. In the Fig. 2 schematic, downward (upward) vertical velocities are positive (negative). Similarly, we use the convention that Doppler velocities are positive (negative) when receding from (approaching) the radar. Using $U$, $V$, and $W$ to represent along-track, cross-track, and vertical direction air parcel velocities (as indicated in Fig. 2), respectively, and using $W_D^H$ to represent the Doppler velocity of the probed hydrometeor mixture, the two line-of-sight velocities measured by the radar are given by

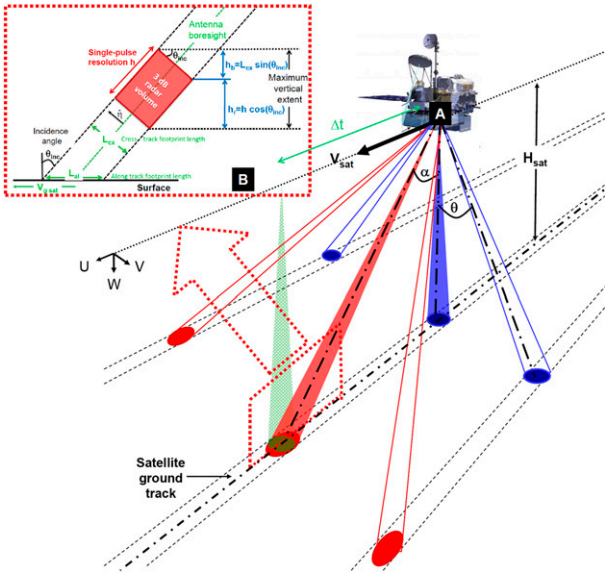


FIG. 2. Scanning geometry for dual-beam radar with three tracks ($N_T = 3$) at beam positions $j = 1, 2, N_T$ (where $\theta_1 = -\theta$, $\theta_2 = 0$, $\theta_3 = \theta$, respectively). Blue (red) beams illustrate cross-track scanning geometries for nadir-view configuration (forward-view configuration). Satellite height and on-orbit satellite velocity are represented by $H_{\rm sat}$ and $V_{\rm sat}$, respectively. Green represents volume of the central-track nadir beam position shift after time $\Delta t \approx H_{\rm sat}\tan(\alpha)/V_{\rm sat}$ has passed (assuming a flat surface between nadir-view and forward-view beams). Inset in top-left-hand corner shows geometry of pulse volume for off-nadir incidence. (See discussion in text for further explanation of the diagram.)

$$V_1 = V\sin\theta + (W_D^H + W)\cos\theta$$
$$V_2 = U\sin\alpha + V\sin\theta\cos\alpha + (W_D^H + W)\cos\alpha\cos\theta. \quad (1)$$

From this equation pair, the along-track (i.e., horizontal) wind velocity is found by

$$U = \frac{V_2 - V_1\cos\alpha}{\sin\alpha}, \quad (2)$$

for which the corresponding standard deviation of the estimate ($\sigma_U$) can be expressed by

$$\sigma_U = \frac{\sqrt{\sigma_{V_2}^2 + \sigma_{V_1}^2\cos^2\alpha}}{\sin(\alpha)}. \quad (3)$$

### *a. Number of tracks*

In an optimal configuration, it would be desirable for a spaceborne Doppler stereoradar to have a large swath made possible by use of scanning (i.e., by allowing for multiple tracks, or identically multiple beam positions,

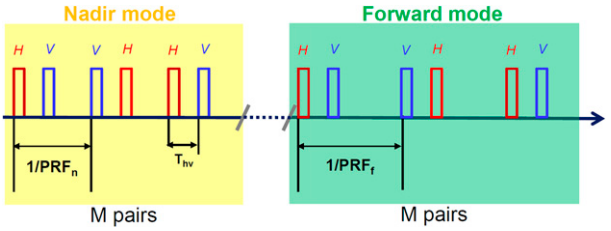


FIG. 3. Pulse scheme envisaged for Doppler stereoradar system: cycle of polarization diversity pairs emitted for nadir view is alternated with cycle of pairs emitted for forward view. Terms H and V denote polarizations along horizontal and vertical polarimetric axes (not indicated), respectively. Note $T_{hv}$ represents pulse-pair time interval. PRF is different for two cycles in order to allow for different unambiguous ranges and equalization of sampling count ($M$) transmitted for each view. Note that when the scanning option is invoked (i.e., $N_T > 1$), two cycles are repeated $N_T$ times.

along each scan). However, the number of tracks is limited by the requirement for a sufficient number of samples needed for reducing the uncertainty in the Doppler velocity measurements. The scanning configurations arising from the nadir-view and forward-view modes can be best perceived as two interlaced modes, each with their own (staggered) pulse-pair repetition frequency (PRF), that is, $\mathrm{PRF}_n$ and $\mathrm{PRF}_f$, respectively, as depicted in Fig. 3.

Radars systems are affected by range ambiguities (Doviak and Zrnić 1984), with the maximum unambiguous range related to the PRF by $c/(2\mathrm{PRF})$, with $c$ being the speed of light. Spaceborne radars developed for atmospheric viewing are typically designed to have an observation window (column) extending over the entire troposphere, and if mirror imaging is desired when used over water, including the near subsurface. Given the stereoradar observation geometry proposed here, setting $\mathrm{PRF}_f \approx \cos\alpha \mathrm{PRF}_n$ guarantees unambiguous acquisitions of dual atmospheric profiles with equivalent height ranges for the two viewing directions. If we assume that an equal number of samples $M$ are to be acquired in the nadir and forward directions, in order to achieve comparable radar return accuracies, then the total dwell time required for full cross-track scans consisting of $N_T$ tracks (i.e., beam positions) for both nadir-view and forward-view configuration modes is $N_T[(M/\mathrm{PRF}_n) + (M/\mathrm{PRF}_f)] \equiv N_T(M/\mathrm{PRF}_e)$, where $\mathrm{PRF}_e$ is an effective PRF obtained from the two directional PRFs akin to the parallel-circuit resistance arising from two separate resistors. The total dwell time needs to be less than the time it takes for the satellite to move along track between an instantaneous pair of nadir-view and forward-view beam positions. This leads to the following constraint for the $M$ samples that are to be acquired in

$$MN_T < \frac{L_{\mathrm{al}}^n \mathrm{PRF}_e}{V_{\mathrm{g\,sat}}} \equiv \xi, \tag{4}$$

where $L_{\mathrm{al}}^n$ is the along-track nadir beamwidth (i.e., from the smallest of the two viewing modes, as evident in Fig. 2) and $V_{\mathrm{g\,sat}}$ is the satellite ground-track velocity. Results for representative values of $\xi$ are given in Table 1. As discussed in section 4b, more stringent constraints would be required for certain conditions, which effectively reduces the threshold value $\xi$ with respect to the product $MN_T$.

### b. Polarization diversity

The stereoradar concept proposed here has been complemented with *polarization diversity* (PD) capabilities that, though technologically more challenging and costly, are concomitantly highly beneficial when employed on a fast-moving spaceborne Doppler millimeter-wave radar (Kobayashi et al. 2002; Battaglia et al. 2013). This issue is best addressed by first noting that space-radar observations of mesoscale convective systems, such as hurricanes, are especially challenging for the three following reasons:

(i) The extreme velocity characteristics of these weather systems require large Nyquist velocities to facilitate the underlying Doppler velocity unfolding calculations. When adopting single-polarization methods, this requirement favors high PRFs, although at 94 GHz, even a PRF as high as 10 kHz only produces Nyquist velocities of 7.5 m s$^{-1}$.

(ii) The vertical extents of these weather systems can exceed 18 km (e.g., convection in slow-moving hurricane eyewalls). When adopting single-polarization methods, this poses an upper bound on the PRF; that is, a PRF of less than $c\cos\alpha/2h_{\mathrm{col}}$, where $h_{\mathrm{col}}$ is the height of the science data column. To guarantee observing the lowest portion of the column (i.e., the surface level) as well as the upper portion of the column (i.e., a cloud-free stratospheric level somewhere in the vicinity of 25–30 km), the maximum PRFs must be on the order of 5–6 and 3.5–4.2 kHz for nadir and forward ($\alpha = 45°$) viewing, respectively.

(iii) The strong turbulence encountered within these systems along with the Doppler fading introduced by radar platform motion significantly broadens the Doppler spectra and reduces the radar decorrelation times (Kobayashi et al. 2002), defined as $T_d \equiv \lambda/(2\sqrt{2}\pi\sigma_D)$, where $\lambda$ is the radar wavelength and $\sigma_D$ is the Doppler spectral width. It should be recognized that decorrelation times

TABLE 1. Stereoradar concept: radar system parameters. Numbers in bold correspond to the nadir view.

| Satellite height | 500 km ($V_{sat}$ = 7.61 km s$^{-1}$; $V_{g\,sat}$ = 7.06 km s$^{-1}$) | |
|---|---|---|
| Angle between beams at surface | 45° (i.e., forward scanning angle = 41°) | |
| Frequency (GHz) | 35 | 94 |
| Peak power (kW) | 1 | 1 |
| Antenna diameter (m) | 3/5 | 1.5/3 |
| Antenna beamwidth (°) | 0.20/0.12 | 0.14/0.07 |
| Footprints* $L_{cx} \times L_{al}$ (km$^2$) | 1.75 × 2.47/1.05 ×1.48 | 1.22 × 1.72/0.61 × 0.86 |
| Spectral width (satellite motion; ms$^{-1}$) | 5.6/3.4 (**8.0/4.8**) | 3.9/2.0 (**5.6/2.8**) |
| Pulsewidth ($\mu$ s) | 3.3 | 3.3 |
| Effective vertical resolution $h_e$ (m) | 1334/895 (**500**) | 997/660 (**500**) |
| PRF (kHz) | 3.6 (**5**) | 3.6 (**5**) |
| Unambiguous height (km) | 30 | 30 |
| $\xi$ [as defined in Eq. (4)] | 523/314 | 365/182 |
| Total system losses (dB) | 5 | 6 |
| Noise figure (dB) | 5 | 5 |
| Single-pulse MDT (dB$Z$) | 1.7/-2.7 (**−1.0/−5.4**) | −8.9/−14.9 (**−11.6/−17.6**) |

* Footprints are expressed for the central-track forward view only with the first (second) number referring to cross-track (along track) resolution.

down to 50–60 $\mu$s could be expected for spaceborne millimeter-wave radar observations of deep convection. PRFs of 5–6 kHz (3.5–4.2 kHz), conforming to values given above for nadir (forward) viewing, correspond to distances between pulses of 166 and 200 $\mu$s (between 238 and 286 $\mu$s), which are incompatible with the previously mentioned short coherency times.

The use of PD, as described by, for example, Pazmany et al. (1999) and Bluestein et al. (2004), offers an effective solution to the first two issues, typically referred to in the literature as the ''range–Doppler dilemma'' (see Doviak and Zrnić 1984). The pulse scheme envisaged for use with a PD capability is shown in Fig. 3. Sending out pairs of H–V pulses at short time intervals (indicated as $T_{hv}$ in the diagram), or likewise at short distances, with relatively low pulse-pair repetition frequency (also denoted as PRF), effectively decouples the maximum unambiguous range [$r_{max} = c/(2\text{PRF})$] from the Nyquist velocity [$v_{Nyq} = \lambda/(4T_{hv})$]. As a result, PD offers the greatest advantage of nearly eliminating aliasing errors when adopting relatively short H–V pulse intervals. For instance, $T_{hv}$ = 20-$\mu$s (50 $\mu$s) intervals correspond to Nyquist velocities of ±42.8 m s$^{-1}$ (±40 m s$^{-1}$) at 35 GHz (94 GHz). Conversely, selection of the pulse-pair repetition frequency is not driven by the decorrelation of the medium (the Doppler velocity is based on the correlation between the closely spaced H–V pulses) and therefore can be properly tuned to the desired unambiguous window. Finally, with respect to the third issue, given the better coherency between the H–V pulses, PD significantly reduces noise errors compared to standard pulse-pair techniques [see Battaglia et al. (2013) and discussion in section 4a].

One drawback of using a radar capable of PD is that it is subject to cross-talk interference, phase noise, and thermal noise (see Pazmany et al. 1999; Battaglia et al. 2013). While all these effects are uncorrelated to cloud signals (and therefore do not bias the estimated mean Doppler velocity though increasing the standard deviation of the velocity estimate), they do appear (depending on $T_{hv}$) as ''ghost'' reflectivity signals (Battaglia et al. 2013). The identification of the sources of cross talk (i.e., multiple scattering-affected regions, surface echoes, depolarizing targets) is essential for achieving accurate Doppler velocities and to properly mask ghost-contaminated areas in the reflectivity analysis. As suggested in Battaglia et al. (2013), an interlaced pulse-pair mode that measures the cross- and copolar reflectivities can achieve such a goal. The elimination of multiple scattering and ghost-contaminated regions results in a reduction of coverage.

### c. *Technical specifications for stereoview radar using polarization diversity*

Table 1 tabulates the important engineering parameters of the various radar configurations chosen for detailed study (i.e., pairing two antenna aperture sizes with each of two frequencies). In the following, we briefly discuss our choices for the most relevant of these parameters.

- *Frequency:* Two frequencies (35 and 94 GHz) are considered. Lower frequencies, such as Ku band and smaller, are not considered because of their low sensitivities and their inability to unequivocally detect cloud hydrometeors with signal-to-noise ratios (SNR) appropriate for Doppler studies (Kollias et al. 2014). Higher frequencies, such as 35 and 90–95 GHz, are

suited for detecting both light and moderate precipitation (with some restriction on the latter), noting that this entire frequency range experiences significant attenuation once heavy precipitation arises (Matrosov 2005). Between 90 and 95 GHz W-band frequencies are most suited for characterizing cloud hydrometeor properties and wind velocities in nonprecipitating and light-to-moderate precipitating cloud environments (assuming the precipitation layer thickness for moderate precipitation is not large).

- *Antenna diameter:* Two antenna options (small and large apertures) are considered in order to assess the different trade-offs in signal strength detection. Notably, the larger aperture option conforms to antenna sizes proposed for future satellite missions (Tanelli et al. 2010).
- *Pulse width:* A reference value of 3.3 $\mu$s, which corresponds to a radial resolution of 500 m, guarantees capturing the vertical hydrometeor profile with a spatial resolution of 500 m when using center-track nadir-view data (as currently done with TRMM, *CloudSat*, and GPM data). Moreover, the vertical profile of horizontal winds with a spatial resolution of better than 1 km (except for the small aperture antenna Ka-band configuration) can be captured when using stereoview data. For the off-nadir direction, the finite beamwidth causes degradation in the vertical resolution. As described in Meneghini and Kozu (1990), and illustrated with the inset in the top-left-hand corner of Fig. 2, the vertical extent of the pulse volume consists of a component due to the range resolution $h_r$ and a component due to the finite beamwidth $h_b$. A definition of the effective vertical resolution $h_e$ is given in Meneghini and Kozu (1990) as a function of the average response function for the received power along the vertical axis, as indicated by the direction for $W$ in Fig. 2. A good approximation when $h_b > h_r$ is given by $h_e = \sqrt{h_r^2 + h_b^2}$; corresponding results for effective vertical resolutions are given in Table 1. It is apparent that since for slant viewing, $h_b$ is the contribution driving $h_e$, it would not be wise to choose shorter pulses because such a selection would significantly penalize the sensitivity (which increases with the square of the pulse length) without improving the vertical resolution of the horizontal winds.
- *PRF:* In terms of Doppler performance, the selection of the pulse-pair repetition frequency for PD systems is not as critical as for pulse-pair processing (Battaglia et al. 2013), but it is still limited by unambiguous range constraints. Assuming the use of PD, for the forward-looking beam we assume a $\mathrm{PRF}_f$ of 3600 Hz to ensure an unambiguous range of 41.6 km at $\alpha = 45°$ (i.e., ≈30-km unambiguous height window), while for scanning with the nadir-view configuration, a $\mathrm{PRF}_n$ of $\mathrm{PRF}_f/\cos\alpha = 5$ kHz is chosen (see discussion above). As previously noted, in any following discussion we assume that the forward PRF (i.e., $\mathrm{PRF}_f$) should be greater than the nadir PRF (i.e., $\mathrm{PRF}_n$) in order to ensure that the same number of samples are collected for both modes (and thus have the same Doppler velocity uncertainty). Overall, given such characteristics, the radar has an average PRF of 4.2 kHz. When considering the adopted pulse width and the fact that the transmitter must send out a pulse for each frequency, the corresponding duty cycle amounts to 2.8%, which is compatible with current state-of-the-art technology.

## 3. The simulation framework

The radar signal is simulated by an end-to-end spaceborne Doppler radar simulator that has been initially developed for nadir configurations (Battaglia and Simmer 2008; Battaglia and Tanelli 2011) and that has now been extended to account for scanning configurations. The simulator couples a forward radiation model and a radar receiver model (Battaglia et al. 2011, their Fig. 1). The forward radiation model computes the cross- and copolar reflectivities and the ideal (unfolded and noiseless) radar Doppler spectra as measured by a spaceborne radar flying over 3D scenes simulated by highly resolved cloud-resolving models. The forward radiation computations are based on a Monte Carlo module [the Doppler Multiple Scattering Simulator; Battaglia and Tanelli (2011)] that accounts for MS and depolarization effects, two essential features when simulating PD configurations. The contributions to the observed Doppler velocities from the satellite motion, the hydrometeor terminal velocity, and vertical air motion are properly coupled with the viewing geometry and the antenna pattern similarly to what is done in Tanelli et al. (2002, 2004).

### a. Surface modeling

The forward model includes a surface scattering module for sea surface backscattering returns. At slant-viewing angles larger than 10°–20°, Bragg scattering models are more appropriate than Kirchoff approximation for describing the scattering behavior of sea surfaces (Ulaby et al. 1986). Normalized surface radar cross sections $\sigma_0$ are derived by scattering perturbation theories (e.g., Apel 1994; Romeiser et al. 1997) once the wave height spectrum is predicted as a function of the frequency, the polarization, the wind incidence direction, and the relative azimuthal-viewing direction of

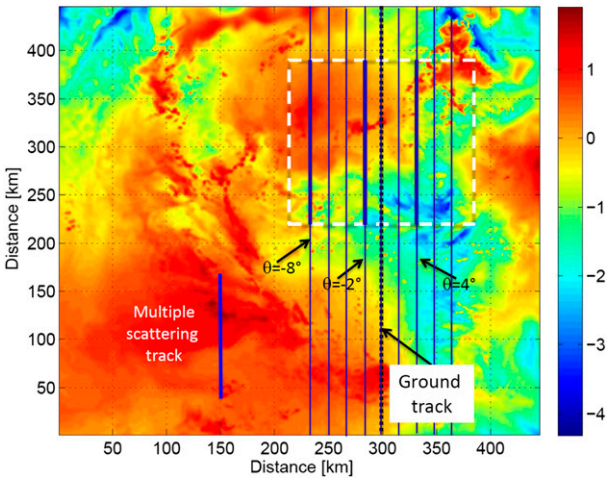


FIG. 4. Column-integrated hydrometeor mass (logarithmic units) for the Hurricane Karl simulation. The push-broom ground projections for a stereoradar scanning over $N_T = 9$ tracks are shown. In this case $\theta = 0°, \pm 2°, \pm 4°, \pm 6°, \pm 8°$ have been considered. The thick blue lines correspond to sections of tracks that are used for specific examples in Figs. 5, 6, 7, 9, 11, respectively.

the radar. Based on measurements at centimeter wavelengths, several parameterizations for the wave spectrum have been developed, which can be used to extrapolate results at millimeter wavelengths. In our simulations we have adopted the model from Apel (1994), which predicts a strong dependence on the wind speed variability at Ka and W bands. The key aspect to be noted here is that, when considering viewing angles larger than 45°, the normalized radar cross sections are at least 30 dB lower than at nadir, with such a difference amplifying for low surface wind speeds. However, measurements of sea and land surface returns at Ka and W bands at incidence angles larger than 20° are almost nonexistent. Such measurements are necessary for the proper modeling and interpretation of the surface echo from scanning millimeter radars and should be conducted during future airborne campaigns.

### b. *Hurricane Karl simulation*

A WRF simulation (Skamarock et al. 2005) of Hurricane Karl on 15 September 2010 when the hurricane was near the Yucatan Peninsula is used as a case study. The 1-km horizontally resolved column-integrated hydrometeor mass WRF field is depicted in Fig. 4. An example of the push-broom scanning pattern is shown in the white inset for the top-right sector of the hurricane. The simulation depicts a variety of cloud types ranging from convective towers to stratiform systems, from shallow precipitation to ice cloud decks, resembling the cloud features shown in Fig. 1. As such it does represent a suitable test scene for assessing the potential of the proposed concept. The vertical variability of the simulated scene is shown in the left panels of Fig. 5 by three along-track profiles of the hydrometeor contents corresponding to the three tracks of Fig. 4. Similarly, the along-track wind vertical profiles are depicted in the right panels of Fig. 5. Red and black contour lines also provide an idea about the intensities of the cross- and vertical winds, respectively. All panels exhibit strong vertical wind shear but with considerable differences in their vertical structure (see first and third tracks in Fig. 5). The convective tower clearly visible in the second panel of Fig. 5 is characterized by strong updrafts (negative $W$) with values exceeding $19\,\mathrm{m\,s^{-1}}$. On the contrary, the warm precipitation cell in the first sector of the third panel (Fig. 5) is not associated with vigorous updrafts.

### c. *End-to-end simulator results*

The forward-simulated radar reflectivities for the three profiles shown in Fig. 5 at Ka and W bands are shown in the left panels of Figs. 6 and 7, respectively. Only the sampling resolution (3-m antenna and 1-km integration), signal attenuation, and the surface echo are considered in the estimation of the forward-modeled radar reflectivities. The corresponding simulated PD radar reflectivities are shown in the right panels of Figs. 6 and 7. For the estimation of the PD reflectivities, the radar receiver noise and ghost images are considered in addition to the factors considered for the estimation of the forward-simulated reflectivities (left panels). The number of PD pairs considered is $M = 17$, which corresponds to the number of samples gathered in each configuration mode at an effective sampling rate equal to $\mathrm{PRF}_e = 2.1$ kHz for a 1-km integration length and for the given number of tracks. In this case it is interesting to see that, because of its lower sensitivity [single-pulse minimum detection threshold (MDT) = 1.7 dB$Z$], the Ka system is missing most of the ice clouds and the shallow convection. The W-band radar has a single-pulse MDT equal to $-15$ dB$Z$; thus, it is capable of detecting all the cirrus clouds and the warm rain cells visible in the bottom row panels (cf. bottom rows of Figs. 6 and 7). In addition to the difference due to the radar sensitivity, the results are affected by the different antenna 3-dB beamwidths (0.2° for the Ka band and 0.07° for the W band). Thus, the surface clutter is spread over a larger vertical extent and all vertical features are smoother in the Ka-band system (cf. the $h_e$ values in Table 1). By comparing the left and the other two columns in Figs. 6 and 7, it is also possible to identify the appearance of ghosts (e.g., at the top of the convective tower in the middle right panel of Fig. 7). Since in our convention the $H$ pulse is emitted first, their appearance is shifted in

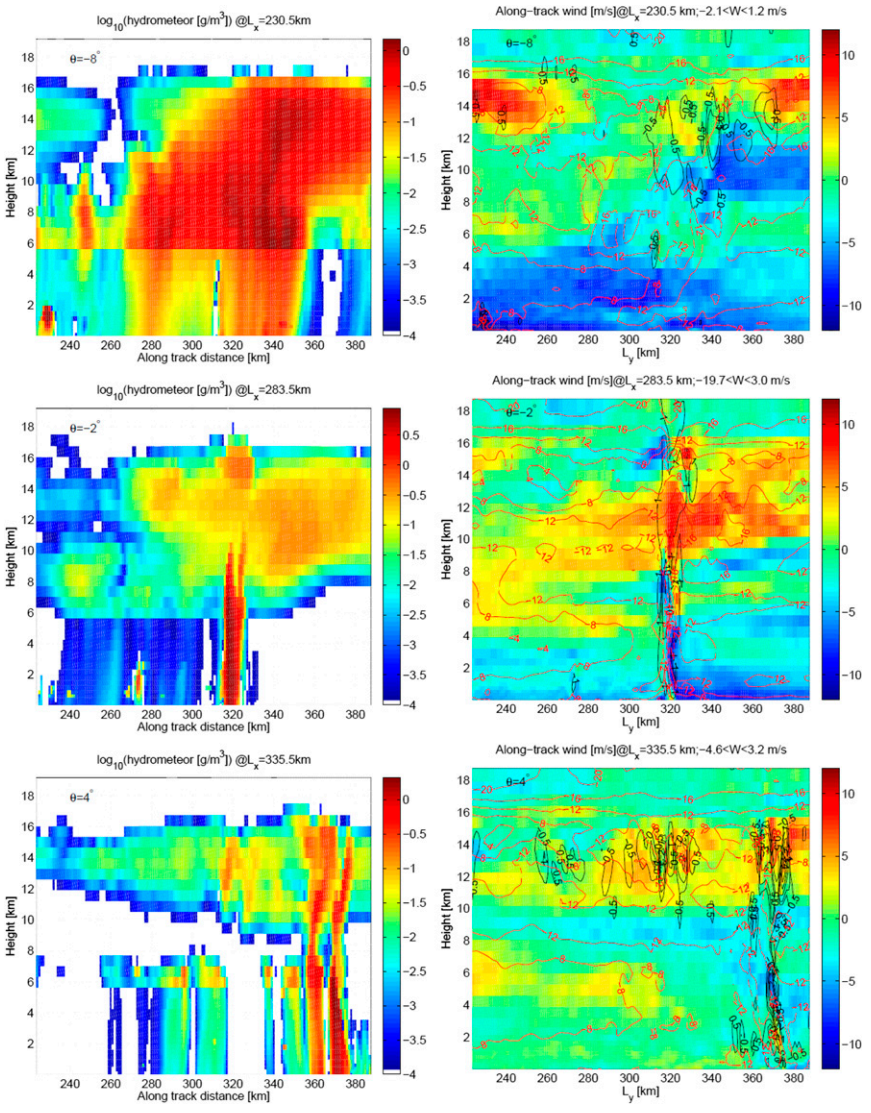


FIG. 5. (left) Hydrometeor contents for the vertical cuts corresponding to the three tracks of the sector illustrated in Fig. 4. (top to bottom) The incidence angle is changing from −8° to −2° to 4°. (right) As in the left panels, but for along-track winds with intensity as indicated in the color bar. Black (red) levels contour the vertical (cross track) wind intensities.

range by a positive (negative) $cT_{hv}/2$ in the plots corresponding to $Z_V$ ($Z_H$) [see Fig. 7 (Fig. 6)].

## 4. Doppler error budget for line-of-sight winds

Doppler measurements are affected by a variety of errors, ranging from errors related to multiple scattering ($\epsilon_{MS}$), NUBF ($\epsilon_{NUBF}$), aliasing ($\epsilon_{aliasing}$), averaging ($\epsilon_{averaging}$), and mispointing ($\epsilon_{pointing}$) to errors strictly related to the noise in the Doppler spectra estimators associated with the specific signal processing ($\epsilon_N$). In first approximation we can assume that the different error sources are independent, so that the total quadratic error ($\epsilon_{TOT}$) can be computed as a quadratic sum of the different errors:

$$\epsilon^2_{TOT} = \epsilon^2_N + \epsilon^2_{NUBF} + \epsilon^2_{MS} + \epsilon^2_{averaging} + \epsilon^2_{aliasing} + \epsilon^2_{pointing} \quad (5)$$

with a similar separation in the different components for the total bias. Note that we will indeed refer to error contributions from NUBF, multiple scattering, and aliasing in Eq. (5) as the residual errors after applying correction/mitigation/dealiasing techniques. To assess the effect of each of these errors, we can exploit our simulation framework which, thanks to the availability of different

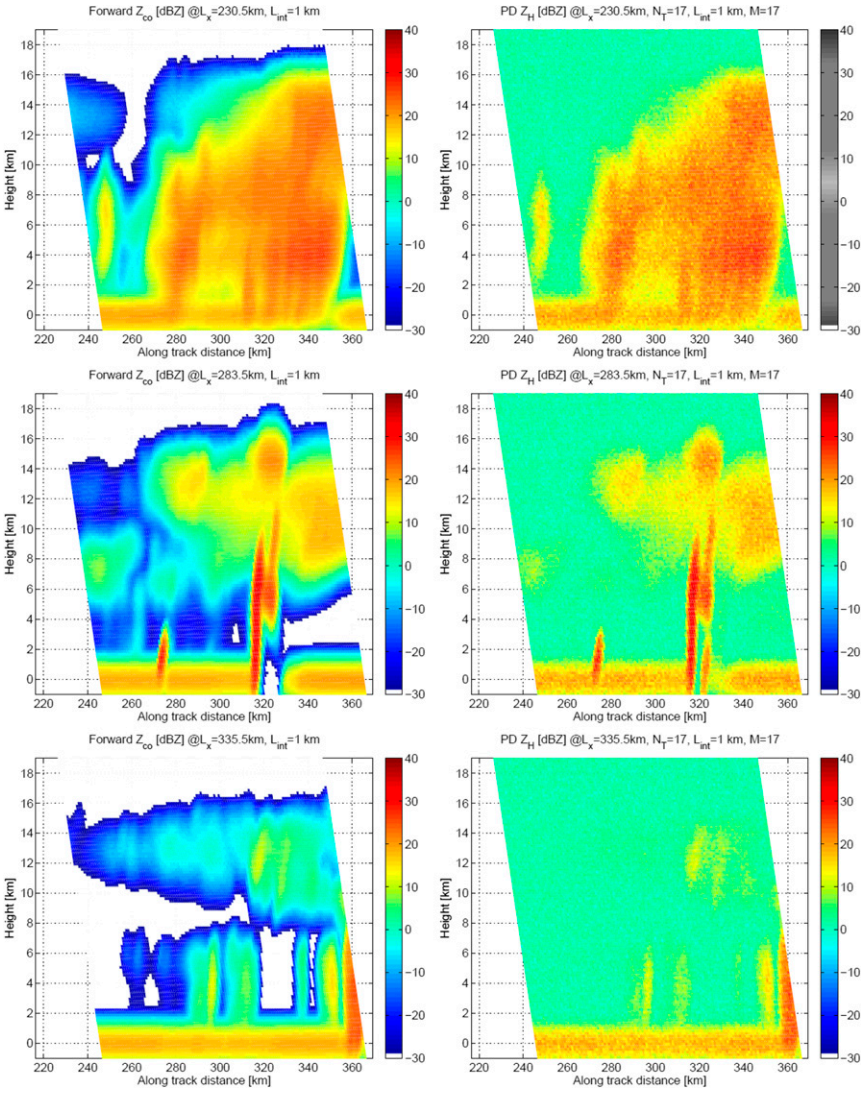


FIG. 6. (left) The 3-m antenna 35-GHz forward reflectivities and (right) the $Z_H$ reflectivities estimated via PD with $T_{\rm hv} = 50\,\mu$s with $M = 17$. The single-pulse MDT is equal to 1.7 dB$Z$ for this system.

spectra, allows isolating and quantifying each error source. We will here discuss only the first four error sources present in Eq. (5). In fact, thanks to the large Nyquist velocities proper of PD systems, residual aliasing errors are deemed negligible, while pointing errors are typically left as requirements for the system pointing stability in order to achieve the science requirements (e.g., see Battaglia and Kollias 2014).

### *a. Noise errors*

The first component of the error budget [Eq. (5)] is probably the best understood. The noise uncertainty in Doppler velocity measurements depends on the single-pulse SNR, the radar Doppler spectrum width, and the number of averaged samples (Zrnić 1977; Kobayashi et al. 2002, 2003). While the SNR depends on the radar sensitivity and the target reflectivity, the number of averaged samples is linearly proportional to the integration time. On the other hand, the radar Doppler spectrum width is generally dominated by the Doppler fading introduced by the satellite motion (Battaglia et al. 2013), which depends on the antenna 3-dB beamwidth and the component of the satellite velocity onto the plane orthogonal to the boresight, that is, along the direction $\hat{\eta}$ (see inset in the top-left corner of Fig. 2):

$$\sigma_D^{\rm sat} = \frac{\theta_{\rm 3dB} V_{\rm sat}^{\hat{\eta}}}{4\sqrt{\log(2)}}. \tag{6}$$

Such Doppler fading is reported in Table 1 for the different configurations analyzed in this work. As a result

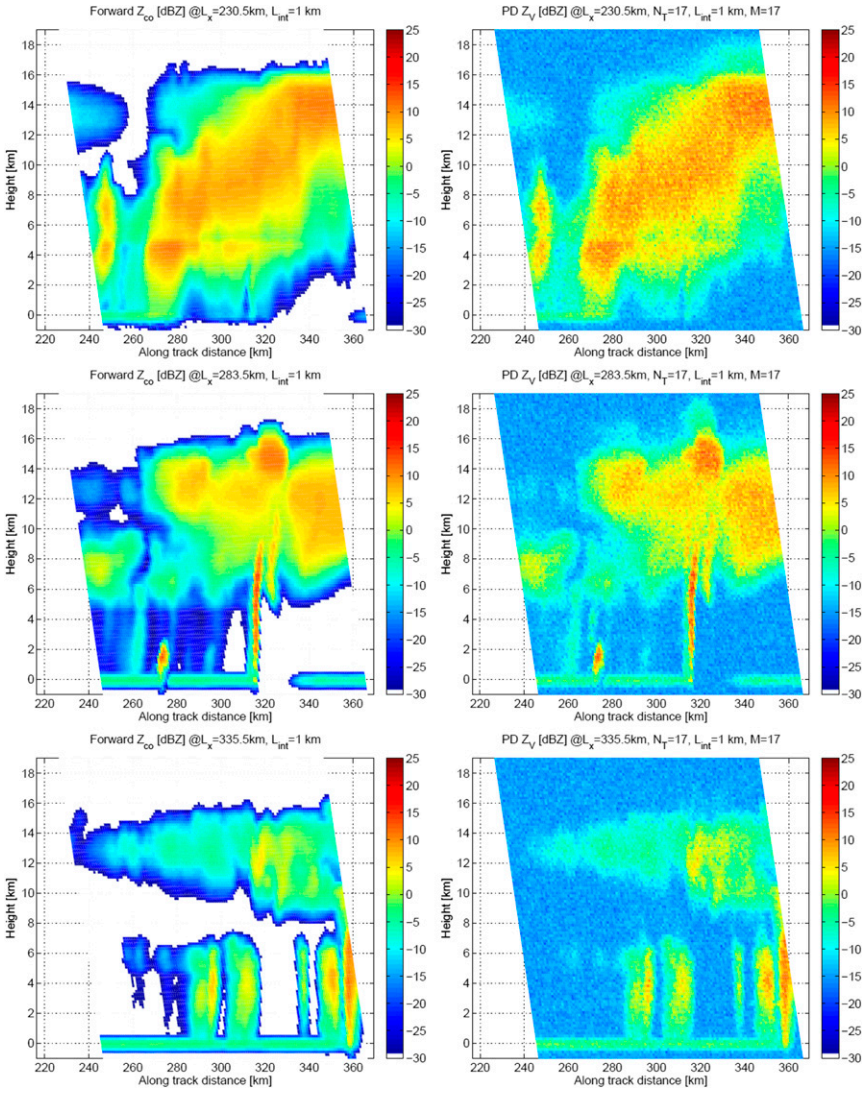


FIG. 7. (left) The 3-m antenna 94-GHz forward reflectivities and (right) the $Z_V$ reflectivities estimated via PD with $T_{hv} = 25\,\mu$s with $M = 17$. The single-pulse MDT is equal to $-15$ dB$Z$ for this system.

of the dependence on $V_{sat}^{\hat{\eta}}$, the Doppler spectral fading induced by satellite motion changes according to the scanning angle and the antenna size, with slant-viewing angles/larger antennas characterized by smaller spectral widths. Noise errors expected for the systems, the specifics of which are listed in Table 1, and for an integration length of 1 km are shown in Fig. 8 for the forward-looking configuration. Results for the nadir-view configurations are very similar (not shown) with the PD accuracy being slightly worse due to the increase in $\sigma_D$, and the pulse-pair accuracy is almost the same for the compensating effect of the increase in PRF and in $\sigma_D$. For the 35-GHz systems (left panel) results for a pulse-pair system with the same PRF are depicted as well (continuous line and dashed lines). PD outperforms the pulse-pair system; while this is unequivocal at 94 GHz, it is less obvious at 35 GHz, especially at low SNR and with small $\sigma_D$. However, if $T_{hv}$ larger than 40–50 $\mu$s are considered, then the advantage of PD with respect to Doppler accuracy is clear at 35 GHz as well, not having mentioned the issues related to the reduction in the Nyquist interval characteristic of pulse-pair configurations [e.g., $\pm 7.7$ (10.7) m s$^{-1}$ with a PRF equal to 3.6 (5) kHz]. From the plots in Fig. 8, it is clear that an appropriate selection of $T_{hv}$ is recommended in order to minimize the noise errors. Values of $T_{hv}$ between 10 and 20 $\mu$s and above 40 $\mu$s seem more appropriate at W band and Ka band, respectively. The selection of $T_{hv}$ affects the position of the blind layers (Kobayashi et al. 2002), which can be identified with a linear depolarization ratio

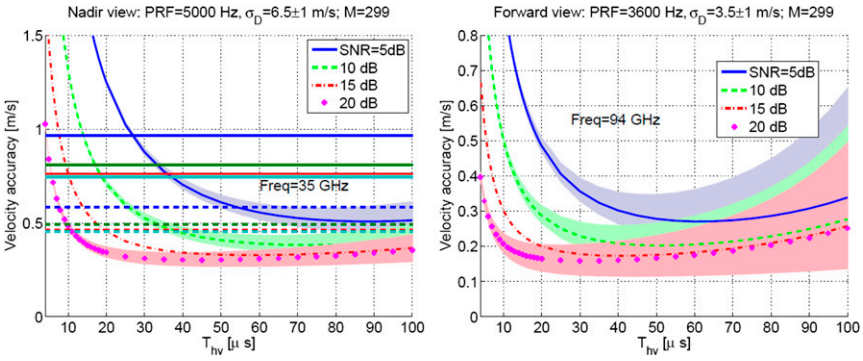


FIG. 8. Noise error in PD estimates as a function of the pulse-pair interval, $T_{hv}$, for different SNRs and with PRFs as specified in the titles. The integration length is assumed to be 1 km for $N_T = 1$. If more tracks are considered, the results worsen with $\sqrt{N_T}$. Lines correspond to the central value of the spectral widths as specified in the title, with the shadowing spanning the $\sigma_D$ interval (i.e., $\pm 1\ \mathrm{m\ s^{-1}}$). (left) For the Ka-band option, continuous and dashed horizontal lines correspond to the pulse-pair (PP) accuracies associated with the central and lower values of $\sigma_D$, respectively. (right) The PP results are not plotted in the W-band case because they produce very bad accuracies, way out of the interval used in the $y$ axis.

(LDR)-interlaced mode [for more details on this, see the discussion in Battaglia et al. (2013)]. Reflectivity fields corresponding to the blind layers could be partially recovered by the noisier LDR mode. The Doppler velocity field will also appear noisy in such regions, especially in the presence of strong reflecting surfaces and low attenuation in the lower atmosphere. However, over ocean and at slant-viewing angles, the surface blind layer returns will be highly suppressed by the expected decrease in the surface normalized backscattering cross section.

### b. *Nonuniform beamfilling errors and no uniform beamfilling correction*

In fast-moving spaceborne Doppler radar, inhomogeneities in the radar reflectivity field within the radar sampling volume can introduce a significant source of error in Doppler velocity estimates (Tanelli et al. 2002). For slant-looking radars, the relevant inhomogeneities are those along the direction $\hat{\eta}$ (see inset in the top left corner of Fig. 2), which corresponds to the along-track direction for nadir-pointing systems. As a consequence, for off-nadir configurations, NUBF effects will be linked not only to along-track reflectivity gradients but also to vertical reflectivity gradients. Thus, NUBF errors will be exacerbated in regions with strong vertical gradients (like in correspondence to horizontal cloud boundaries, the bright band, or strongly attenuating media). For instance, a perfectly horizontally homogeneous attenuating rain layer will appear to fall slower than its actual Doppler velocity when observed by the forward-looking beam, whereas its Doppler velocity will be unbiased when observed by the nadir beam.

NUBF corrections are possible only when the reflectivity gradient along the $\hat{\eta}$ direction, $\nabla_{\hat{\eta}} Z$, can be properly estimated. In a stereoradar configuration this is certainly possible, with the additional condition that the radar footprint is properly oversampled for accurately estimating such quantity. This requires more stringent constraints on the value of $\xi$ defined in Eq. (4). Oversampling half of the footprint—a reasonable assumption—will reduce by a factor of 2 the value expressed in Eq. (4) and reported in Table 1. As demonstrated in Schutgens (2008) and Sy et al. (2013), the correction to the Doppler velocity is given by

$$V_{\mathrm{Dop,CORR}} = V_{\mathrm{Dop,OBS}} - \beta \nabla_{\hat{\eta}} Z, \tag{7}$$

where $\beta$ is a coefficient depending on the specific configuration. By generalizing the procedure described in Sy et al. (2013) for Gaussian circular antennas, the $\beta$ coefficient is typically bounded between

$$\beta_{\mathrm{linear}} = \frac{V_{\mathrm{g\,sat}}^{\hat{\eta}}}{d_g} \frac{\log(10)}{40\log(2)} \rho_x^2 = \frac{\log(10)}{160\log(2)} V_{\mathrm{g\,sat}} H_{\mathrm{sat}} [\tan(\theta_{3\mathrm{dB}})]^2 \quad \text{and} \tag{8}$$

$$\beta_{\mathrm{step}} = \frac{V_{\mathrm{g\,sat}}^{\hat{\eta}}}{d_g} \frac{\log(10)}{10\sqrt{2\pi}\log(2)} \rho_x^2 = \frac{\log(10)}{40\sqrt{2\pi}\log(2)} V_{\mathrm{g\,sat}} H_{\mathrm{sat}} [\tan(\theta_{3\mathrm{dB}})]^2, \tag{9}$$

where $\rho_x$ is the radius corresponding to the 3-dB beamwidth, $d_g$ is the distance between the satellite and the ground along the boresight, and $V_{\mathrm{g\,sat}}^{\hat{\eta}}$ is the

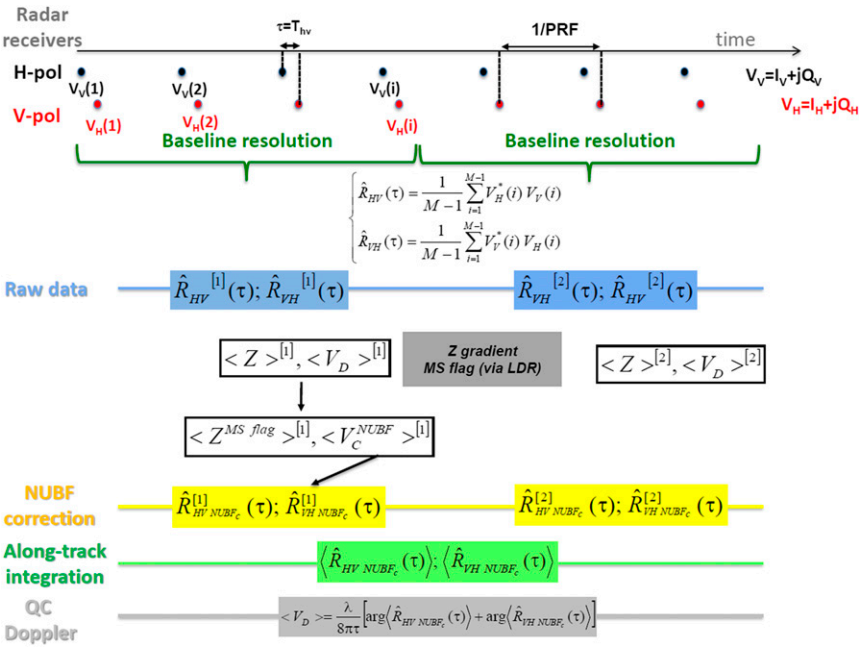


FIG. 9. NUBF correction procedure illustrated for a given range bin. The $I$ and $Q$ time series at the two receivers are used to estimate the VH and HV correlations at lag 1 with $\tau = T_{hv}$ (''raw data''). This is done at a baseline resolution that is optimal to compute along-track reflectivity gradients. The phases in $I$ and $Q$ are properly corrected, and the correlation functions are recomputed accounting for NUBF (''NUBF correction''). Then the corrected correlation functions are averaged in order to achieve the desired integration length (''along-track integration''). Quality-controlled mean Doppler velocities (''QC Doppler'') can be produced at the end of the processing chain.

ground-track satellite velocity along $\hat{\eta}$. For instance $\theta_{3dB}$ values of 0.07°, 0.12°, and 0.2° and $H_{sat} = 500$ km correspond to $\beta_{linear}$ of 0.11, 0.32, and 0.89 m s$^{-1}$ (dB km$^{-1}$)$^{-1}$ and $\beta_{step}$ of 0.15, 0.43, and 1.2 m s$^{-1}$ (dB km$^{-1}$)$^{-1}$; consequently, the larger $\theta_{3dB}$ the larger the NUBF correction. Within our simulation framework, the step coefficient reported in Eq. (9) produces better corrections and is used to perform the NUBF correction. The overall NUBF correction procedure follows several steps, as illustrated in the flowchart depicted in Fig. 9.

1) First, along-radial (toward the radar) and along-track gradients ($\nabla_r$ and $\nabla_{al}$, respectively) are estimated at a fixed baseline (which should be comparable with the footprint).
2) Term $\nabla_{\hat{\eta}} Z$ is derived as a linear combination of the previous two:

$$\nabla_{\hat{\eta}} Z = \frac{1}{\cos\alpha}\nabla_{al} Z + \frac{\sin\alpha}{\cos\alpha}\nabla_r Z. \qquad (10)$$

3) Then, the NUBF velocity bias is computed according to Eq. (7) with the $\beta$ coefficient expressed in Eq. (9).
4) This velocity bias is transformed into a proper phase shift $[\Delta\Psi = -(\pi\beta\nabla_{\hat{\eta}} Z/v_{Nyq})]$ and the correlation functions are corrected accordingly.
5) Finally, Doppler estimates are performed at any integration length (Sy et al. 2013).

To assess the quality of the NUBF correction, we use the forward SS Doppler velocities computed with the satellite velocity set to 0 m s$^{-1}$ as a touchstone. An example is presented in Fig. 10 where the reference velocities (left column) are compared with the pulse pair polarization diversity (PPPD)-estimated Doppler velocities before (middle column) and after (right column) NUBF correction. The overall biases and standard deviations reported in the insets in the top-right corners clearly improve when the NUBF correction is implemented. This is particularly true for the smallest antennas and at the lowest frequency when NUBF errors are larger.

### c. *Multiple scattering errors*

Multiple scattering [for a comprehensive review of the topic, refer to Battaglia et al. (2010)] is likely to affect the radar signal in presence of thick dense ice layers and in strong convective cores. For instance in

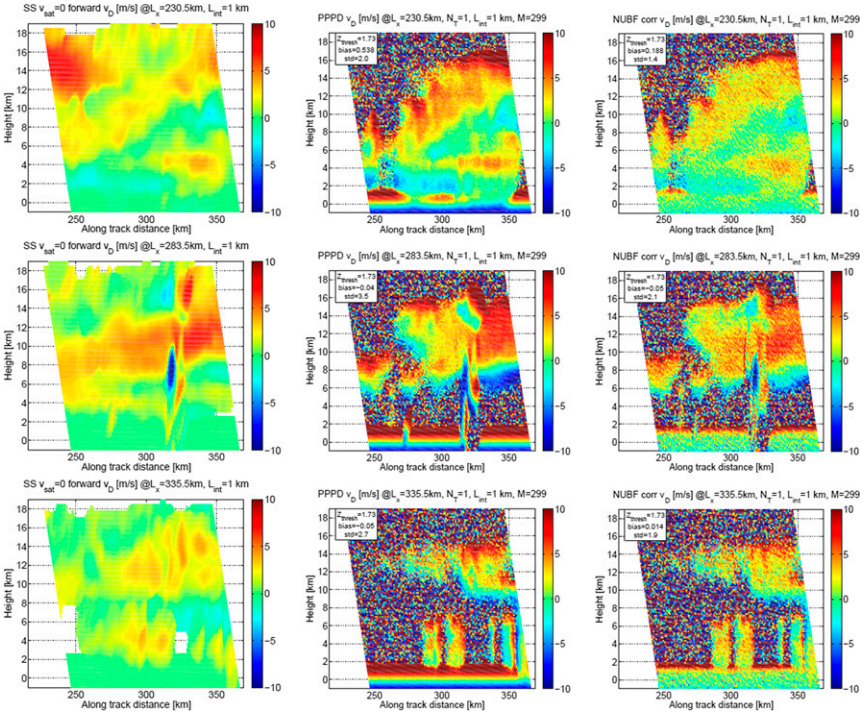

FIG. 10. (left) The 35-GHz single-scattering forward Doppler velocities with no satellite motion for the $Q_4$ sector and the three tracks illustrated in Fig. 6. (middle) PPPD-estimated Doppler velocity with $N_T = 1$ and $L_{\text{int}} = 1$ km. (right) As in the middle column after the NUBF correction.

Fig. 1, the region of the eyewall indicated by the arrow shows a clear example of pulse stretching in proximity to the surface, an unequivocal signature of multiple scattering (Battaglia and Simmer 2008; Battaglia et al. 2014). According to the criterion proposed by Battaglia et al. (2008), all the profiles with one-way path integrated attenuation exceeding 15 dB (and connected by a continuous line) are contaminated by significant multiple scattering at heights below the white line. The track depicted in blue in the bottom-left part of Fig. 4 is characterized by large hydrometeor contents (top-left panel in Fig. 11) and is therefore quite interesting for discussing multiple scattering-related errors. In Fig. 11 we show results for the 3-m W-band antenna in the forward-view configuration. There is an obvious region with strong attenuation corresponding to distances beyond the 100-km marker. Note the similarities with the region around a latitude of 20° observed by *CloudSat* in Fig. 1. This region is affected by significant multiple scattering: in fact, as shown in the middle-right panel, multiple scattering reflectivity enhancements can exceed 10 dB. In correspondence of such a region of strong multiple scattering enhancement, the line-of-sight Doppler velocities also significantly depart from the single-scattering (SS) Doppler velocities (middle-left and bottom-left panels). Errors larger than 2 m s$^{-1}$ can be observed within multiple scattering producing clouds. This is in agreement with previous findings by Battaglia and Tanelli (2011). Our recommendation is therefore to avoid the use of the Doppler velocity within multiple scattering contaminated regions, which again can be easily identified if an LDR mode is available. As already demonstrated in Battaglia et al. (2007), large LDR values are a signature of multiple scattering (see bottom-right panel). An LDR threshold around −10 dB seems sufficient to mask out multiple scattering contaminated profiles and will be used in the next error budget analysis.

### d. *Averaging errors*

While averaging along track is generally considered useful for reducing the noise error, it introduces an additional error source as well. With the term ''averaging'' error, we will refer then to the additional error introduced when averaging over distances where winds are not uniform either because of intensity or direction, for example, regions with strong along-track wind shears or in the proximity of convective cores. The averaging error that appears in Eq. (5) can be derived from a direct comparison between the high- and the low-resolution radial winds computed by the forward model and re-interpolated at the highest resolution. Examples of such

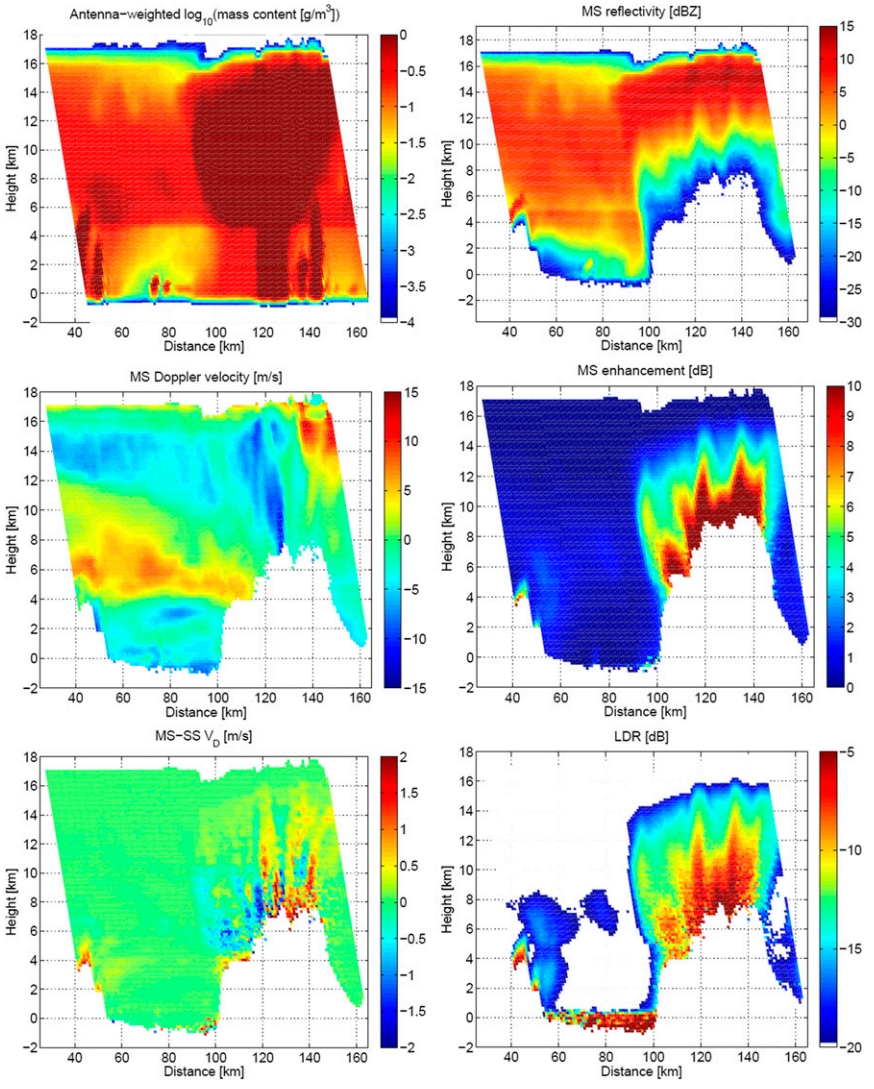


FIG. 11. Example of multiple scattering effects for the 3-m W-band radar configuration and for the forward track corresponding to the black line depicted in Fig. 4. (top left) Hydrometeor content and (top right) measured reflectivity. (middle left) Multiple scattering Doppler velocity and (right) multiple scattering reflectivity enhancement. (bottom left) Doppler velocity multiple scattering error and (bottom right) LDR.

errors are shown in Fig. 12. As expected averaging errors increase with the integration length (cf. different lines in the left panel) and are more important in regions where the wind field changes over scales that are smaller than the integration length (e.g., at about 330 km in correspondence to the convective core). As shown in the right panel, when strong variability of the wind fields is encountered, it can introduce error locally exceeding $2\,\mathrm{m\,s^{-1}}$ already with a 5-km averaging. For the example shown in Fig. 12, the averaging error for the overall scene amounts to $0.73\,\mathrm{m\,s^{-1}}$. Thus, this error cannot be neglected in the velocity error budget quantification.

### e. *Overall error budget*

The overall error statistics for the line-of-sight Doppler velocities for the four stereoradar configurations examined in this study (two frequencies plus two antennas) are summarized in Fig. 13. Total errors (continuous lines) are computed by using as a reference the SS Doppler velocity at $V_{\mathrm{sat}} = 0$ and including all the simulations. Only pixels with SNR $> 3$ dB and with ghost ratios—as defined in Battaglia et al. (2013)—above 0 dB have been considered. Results with $N_T = 1$ and $N_T = 17$ (red and black lines, respectively) are

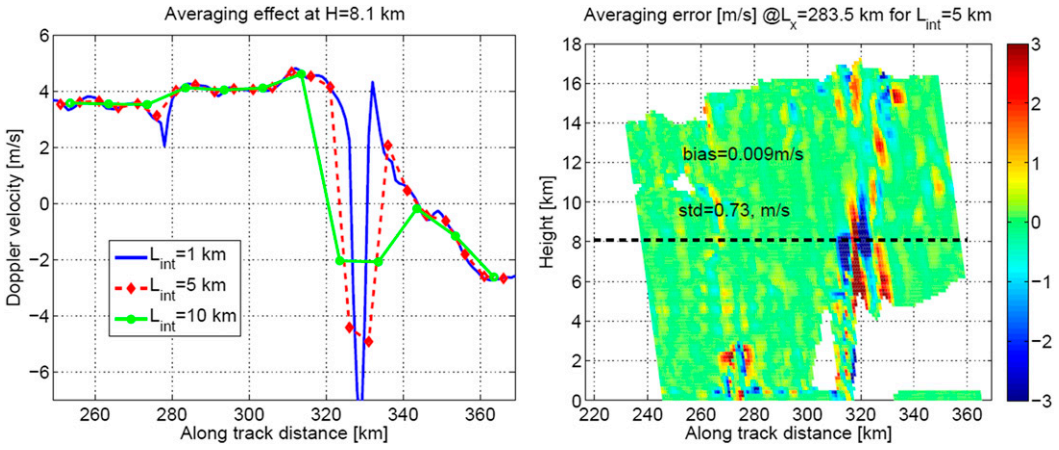


FIG. 12. Averaging effect corresponding to the second track shown in Fig. 5 and at a height of (left) 8.1 km and (right) averaging errors for the entire curtain (the dashed line corresponds to the profile shown in the left panel) for an integration length of 5 km and for reflectivities above −30 dB$Z$. Standard deviations and biases for the averaging errors are also provided.

reported as a function of the integration length (ranging from 1 km, the cloud model resolution, to 10 km). With the same antenna size, errors are much larger at 35 than at 94 GHz (cf. top-right and bottom-left panels, respectively). This is expected because of the larger noise and NUBF errors associated with the lower frequency. By the same token, at the same frequency, larger antennas produce much better results (cf. left and right panels). However, the 5-m 35-GHz configuration has similar performances to the 1.5-m 94-GHz configuration (top-left and bottom-right panels, respectively). Generally, the noise error (dashed lines) is dominating at short integration lengths and large $N_T$, while the NUBF errors tend to dominate at long integration lengths and low $N_T$. The NUBF correction is indicated by the arrows, with a reduction (increase) in the standard deviation error when arrows are pointing downward (upward). Except at large $N_T$ and low integration lengths (when reflectivity gradient estimates are noisy), the NUBF correction is decreasing the overall standard deviation. This effectively corresponds to a reduction in biases localized in regions with strong reflectivity gradients. As expected the correction is more important at 35 GHz and for smaller antennas.

The overall error inclusive of noise, NUBF (residual error after correction), and averaging error is shown as continuous lines in Fig. 13. Note the gap between continuous (total) and dashed (noise) lines: when considering only noise errors, the overall errors can be seriously underestimated. The different behavior of the total and noise errors with respect to the integration length clearly demonstrates the trade-off between averaging and noise errors. For instance, for the 94-GHz 3-m antenna with $N_T = 1$, no reduction in standard deviation error is practically achieved increasing the integration length above 1 km because the overall error is practically dominated by the residual NUBF error (about 0.3 m s$^{-1}$). If the averaging error is included, then the actual total error does actually increase for integration lengths above 1 km for both $N_T = 1$ and $N_T = 17$. This means that integrating for distances longer than 1 km does actually worsen the overall performance and makes no sense for the cases here analyzed. Increasing the along-track integration is not the panacea for spaceborne Doppler radars. This conclusion may be affected by the resolution of the adopted cloud-resolving model (here, 1 km). However, we expect that, when moving toward more highly resolved wind fields, the impact of the averaging error will increase. Results for the nadir viewing (not shown) are 30%–40% better than those for the forward viewing, thanks to a reduced level of noise and NUBF errors. In fact, at vertical incidence, more averaging samples are available due to the higher PRF ($\mathrm{PRF}_n > \mathrm{PRF}_f$) and vertical inhomogeneities are not producing NUBF biases.

As discussed in section 1, accuracies of the order of 2 and 3 m s$^{-1}$ are adequate for horizontal velocity mesoscale dynamic and/or data assimilation studies. When considering that along-track winds are retrieved via Eq. (2) with errors computed according to Eq. (3), it is sensible to require a 1 m s$^{-1}$ accuracy for the forward direction winds to fulfill such a requirement. This threshold has been marked in Fig. 13 by the pale yellow shading. For the 94-GHz configuration with 3-m antenna, the 1 m s$^{-1}$ accuracy requirement at 3-km integration length is achieved already with $N_T = 17$; at the same integration length, the 35-GHz 5-m antenna can achieve an rms accuracy for the along-line-of-sight wind

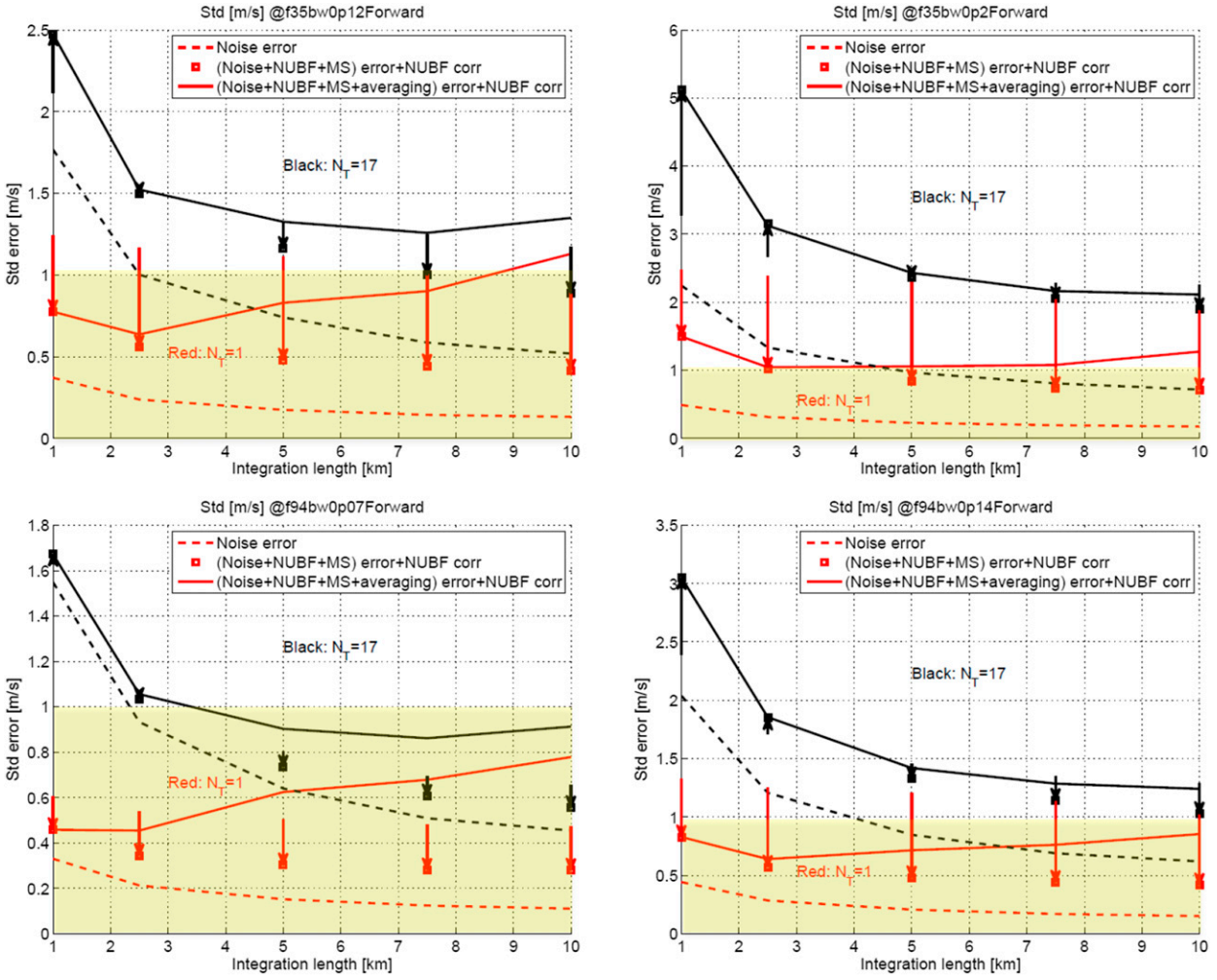


FIG. 13. Total standard deviation error for different configurations for the forward-looking beams. (top) The 35-GHz system with (right) 3- and (left) 5-m antennas. (bottom) The 94-GHz system with (right) 1.5- and (left) 3-m antenna. A PP forward mode at PRF = 3.6 kHz interlaced with a nadir forward mode at PRF = 5 kHz has been considered, which corresponds to 299 H–V pairs for $N_T = 1$ at 1-km integration length. Arrows indicate the amplitude of the NUBF correction. The yellow-shaded areas mark the 1 m s$^{-1}$ accuracy requirement.

of 1.5 m s$^{-1}$. The other two configurations with smaller dishes see a degradation of performances due to a combined effect of larger NUBF, multiple scattering, and noise effects. The two configurations with large antennas have therefore great potential.

Note that here we have not adopted any frequency agility (Amayenc et al. 1993), which could effectively increase $N_T$ (and thus coverage) or improve the accuracy (by increasing the number of averaged samples). For a frequency agile radar, it is possible to transmit pulses closely spaced in time with different "colors" compatibly with the duty cycle (that for our system is currently at about 3%). A system with $N_c$ colors permits either to achieve the same performances on $N_T \times N_c$ tracks or to boost the performances to the level reached by a radar with no frequency agility but scanning only $N_T/N_c$ tracks.

## 5. Retrieval of along-track winds

The stereoradar approach allows a direct retrieval of the along-track winds by linearly combining the nadir viewing and the forward viewing observations via Eq. (2), after properly remapping the nadir sampled into the forward sampled volumes. The only underlying assumption is that the wind field is not changing between the forward and nadir views, which, for the given satellite observation geometry, corresponds to 1-min and 10-s time lags (unless a convoy is considered). This assumption fails in deep convective cores, which may be characterized by wind *e*-folding times of the order of 1 min or less. On the other hand, such convective cores are likely contaminated by multiple scattering and therefore excluded by any Doppler analysis. The

horizontal along-track retrieved winds corresponding to the right panels of Fig. 5 are shown in Fig. 14 for the 5-m Ka radar (left panels) and the 3-m W-band radar (right panels). Results are presented for $N_T = 5$. Retrievals are limited to regions with SNRs above 3 dB and where the ghost ratios are lower than 0 dB. The two radars are properly identifying most of the features of the cloud system, like vertical wind shear or convergence/divergence regions. For instance, note how neatly the two radars detect the dipole wind structure at the top of the convective tower in the middle panels. As expected the 5-m Ka system is characterized by less accurate results and it is limited by its lower sensitivity (e.g., consider the ice cirrus in the bottom-left panel), though in convective cores and strong precipitation areas, it has better penetration capabilities (see, for instance, the feature in the right-bottom corner of the top-right panel). The results from the 94-GHz system in regions of good SNR look stunning. A summary of the performances is reported in Table 2 for the four radar configurations outlined in Table 1 and for the increasing number of tracks ($N_T = 1, 5, 9, 17$). Values marked in italic (bold) correspond to those that satisfy the $3\,\mathrm{m\,s^{-1}}$ ($2\,\mathrm{m\,s^{-1}}$) accuracy criterion. Overall, the 3-m 94-GHz radar can achieve accuracies of the order of 1.3–2.6 $\mathrm{m\,s^{-1}}$ when increasing the number of tracks from 1 to 17. Similarly, the 5-m 35-GHz radar is performing slightly worse (ranging from 1.5 to 3.6 $\mathrm{m\,s^{-1}}$). The other two configurations with smaller antennas produce worse results, with accuracy further deteriorating with increasing $N_T$. This is because NUBF corrections become increasingly less effective with increasing noise levels. For the hurricane scene under analysis, the fractional coverage (relative to the −30-dB$Z$ level) where the along-track wind retrievals are performed is also reported in Table 2. Overall, the 5-m 35-GHz (the 3-m 94-GHz radar) radar has a fractional coverage exceeding 60% (65%). Here, the −30-dB$Z$ level has been selected, for it roughly corresponds to the minimum detectable signal of the *CloudSat* radar (Tanelli et al. 2008) (see also Fig. 1).

Since the scanning Doppler radars here proposed have sensitivities worse than *CloudSat* (cf. the single-pulse MDTs in the last row of Table 1 with the *CloudSat* value of −16.5 dB$Z$), we can use the probability density function of *CloudSat*-observed reflectivities to compute how frequent the proposed systems could detect clouds. Figure 15 depicts the cloud detection as a function of a threshold reflectivity value ($Z_{\min}$) for different cloud types, as classified in the 2B-CLDCLASS (Mace et al. 2007). The analysis is based on an entire year of *CloudSat* data (2007); all pixels below 1 km have been excluded. The fraction is monotonically decreasing with $Z_{\min}$. If only clouds with return above $Z_{\min} = -10$ dB$Z$ are considered, then only about 40% of the clouds detected by *CloudSat* will be visible. This percentage significantly increases if only precipitating systems are considered: for instance, with the same reflectivity threshold, the percentage of detection (with respect to the *CloudSat* coverage) amounts approximately to 60% and 80% for nimbostrati and deep convective clouds, respectively (see crosses and dashed–dotted lines in Fig. 15). This demonstrates that the Doppler radars proposed in this work can provide useful Doppler coverage for systems associated with precipitating systems.

## 6. Conclusions

In this investigation a component-by-component error budget analysis for retrieving along-track winds using a spaceborne Doppler radar concept has been performed. The analysis is conducted using a state-of-the-art spaceborne radar forward radiation model that considers error sources due to nonuniform beamfilling (NUBF), multiple scattering, averaging, and signal noise. The relative importance of these individual errors depends on a complicated interplay between different factors: primarily the scene under observation, the viewing geometry, the scanning configuration, and the adopted integration length. The radiation model is applied over an atmospheric environment generated from a 1-km spatial-resolution WRF simulation of a hurricane, which is effective for providing a realistic cloud setting in which to conduct the error analysis. The proposed spaceborne millimeter-wave Doppler stereoradar uses a dual-beam nadir-view/forward-view design. Conceptually, the instrument is flown on a LEO satellite platform.

Various instrument configurations involving two radar frequencies, 35 and 94 GHz, each equipped with small and large antenna sizes (between 1.5 and 5.0 m) have been examined. In conducting the analysis, radar capabilities are extended to use cross-track scanning, as well as equipping each radar configuration with polarization diversity (PD). In fact, one of the major outcomes of the analysis is that the use of PD helps remove velocity folding error, an important component to any error budget when conducing Doppler velocity retrieval from space. In regard to the four fundamental error sources, the following conclusions can be drawn:

(i) *Signal noise errors* are a dominating error source only if short integration lengths and/or wide-scan swaths are required. Their assessment is straightforward, being based on analytical formulas (e.g., see Fig. 8).

(ii) *Averaging errors* are potentially relevant, particularly for cloud systems experiencing highly variable

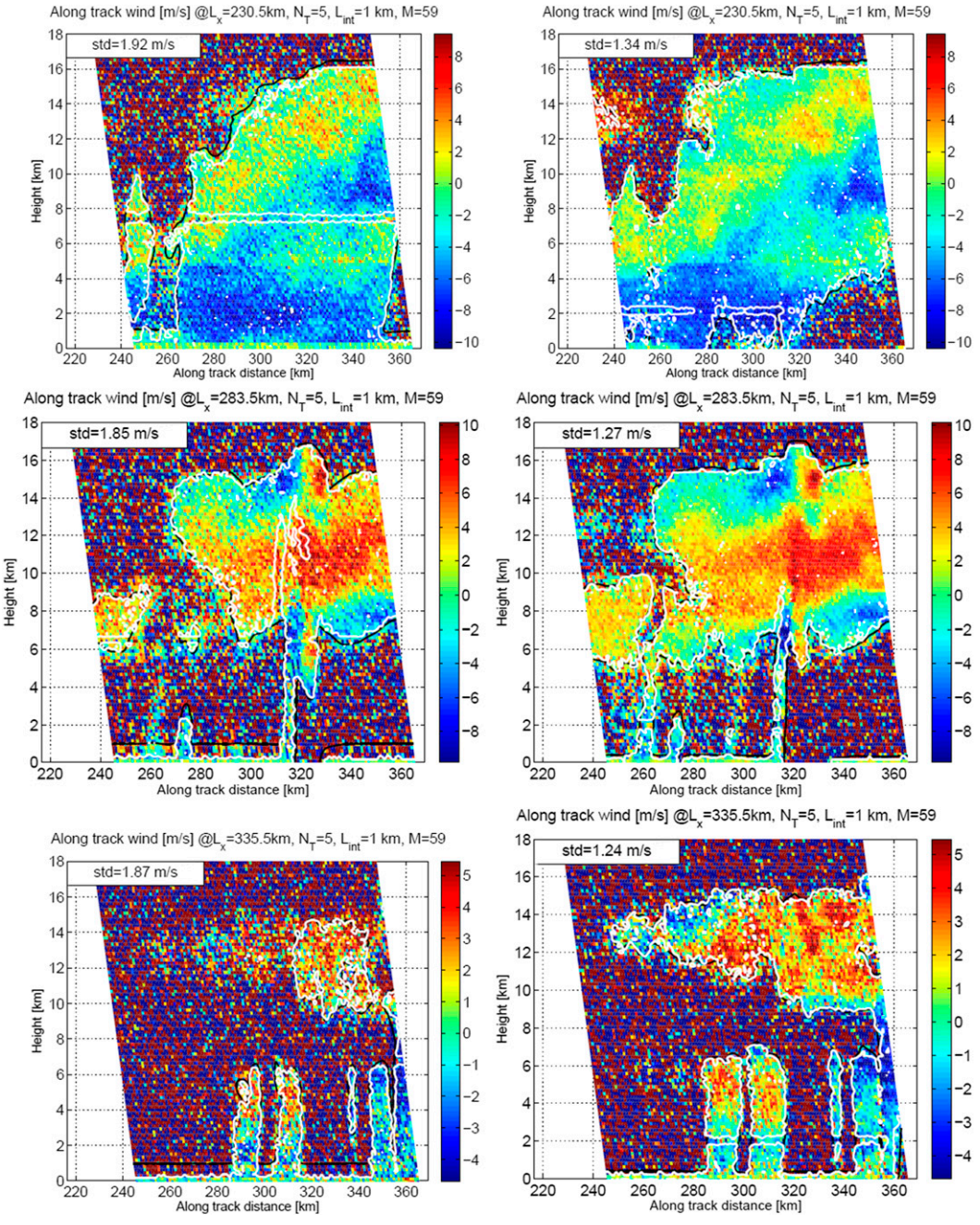


FIG. 14. Retrieved along-track winds (m s$^{-1}$) as indicated in the color bar for (left) a 35-GHz 5-m antenna and (right) a 94-GHz 3-m antenna corresponding to the curtains shown in Fig. 5. Five tracks ($N_T = 5$) and an integration length of 1 km are considered. Black (white) lines contour regions where SNR = 3 dB (ghost ratios are equal to 0 dB). Standard deviation errors corresponding to the whole scene are also reported inside the panels.

wind fields and for radar systems whose overall total error requirement is below 1–1.5 m s$^{-1}$. In such conditions, while averaging over longer integration lengths reduces the signal noise error, it also increases the averaging error, with a concomitant increase in the total error. Ideally, the integration length should be chosen in an adaptive way as a trade-off between the decrease in signal noise error and the increase in averaging error. Research along these lines is now underway in preparation for the EarthCARE mission (see Sy et al. 2014).

(iii) *Multiple scattering errors* are mostly relevant within convective cores and thus in cloud areas producing

TABLE 2. Errors and fractional coverage (relative to the −30-dB$Z$ level) in along-track wind retrievals for the four radar options and for the increasing number of tracks. An integration length of 1 km is assumed. Values marked in italic (bold) correspond to those that satisfy the 3 m s$^{-1}$ (2 m s$^{-1}$) accuracy criterion.

| Configuration | | 35 GHz, 3 m | 35 GHz, 5 m | 94 GHz, 1.5 m | 94 GHz, 3 m |
|---|---|---|---|---|---|
| | Coverage (%) | 61 | 67 | 62 | 74 |
| $N_T = 1$ | $\epsilon_v$ (m s$^{-1}$) | *2.4* | **1.5** | **1.8** | **1.3** |
| | Coverage (%) | 60 | 65 | 60 | 72 |
| $N_T = 5$ | $\epsilon_v$ (m s$^{-1}$) | 4.3 | *2.2* | *2.8* | **1.7** |
| | Coverage (%) | 58 | 64 | 57 | 70 |
| $N_T = 9$ | $\epsilon_v$ (m s$^{-1}$) | 5.6 | *2.7* | 3.5 | **2.0** |
| | Coverage (%) | 54 | 60 | 53 | 65 |
| $N_T = 17$ | $\epsilon_v$ (m s$^{-1}$) | 7.7 | 3.6 | 4.8 | *2.6* |

strong attenuation caused by scattering. Atmospheric profiles contaminated by multiple scattering can be identified with an LDR-interlaced mode. Our recommendation is to flag but not include them in wind analyses.

(iv) *NUBF errors* are a key component of an overall error budget and are particularly relevant at Ka band and for small antennas. These errors are mostly driven by along-track reflectivity gradients for scanning out of the nadir-view configuration, whereas by vertical inhomogeneities for scanning out of the forward-view configuration. This makes it possible to have NUBF errors stemming from horizontally homogenous clouds but in the presence of vertical inhomogeneities (e.g., caused by strongly attenuating hydrometeors or by a melting layer). This situation is applicable to any cloud Doppler scanning radar mounted on a LEO satellite platform. This error can be mitigated against by use of a reflectivity gradient technique, which requires oversampling of the beams. However, this limits the number of available tracks in a stereoconfiguration and thus the coverage. Detailed assessment of this type of error requires the use of a sophisticated three-dimensional Doppler radar simulator and would be essential in a preparatory study for a specific configuration of a Doppler stereoradar deployed on a fast-moving satellite platform.

The error budget analysis procedure has been applied to the proposed Doppler stereoradar design with the aim of assessing its potential for direct reconstruction of along-track wind velocities. The total error results (summarized in Table 2) show that large antennas are the key for success. For instance, retrieval errors can be reduced to 1.3 and 1.5 m s$^{-1}$ at 1-km integration lengths when no scanning is considered for the 5-m Ka-band and 3-m W-band radars, respectively. When scanning is introduced, noise errors become the main driver of the error budget, with the total error roughly increasing with the square root of the number of tracks. This problem can be mitigated against by integrating over longer distances and/or by adopting frequency diversity and/or by improving the SNR (e.g., via pulse compression). By adding information concerning horizontal and vertical dynamics of cloud systems to their microphysical characterization (which has already been demonstrated using incoherent millimeter-wave radars), the proposed spaceborne Doppler stereoradar system could certainly raise our understanding of the earth's water and energy cycles. The proposed design is adaptable to electronically scanned (phased array) radar systems. An operational spaceborne phased-array radar at Ka band has already been flown (i.e., on the GPM satellite), while at W band, current technological advancements will make this approach possible in the near future. This bodes well for extending the capabilities of millimeter-wave Doppler stereoradars in space and thus for continuing the march to better understand how clouds in the atmosphere prevail upon and react to the weather and climate.

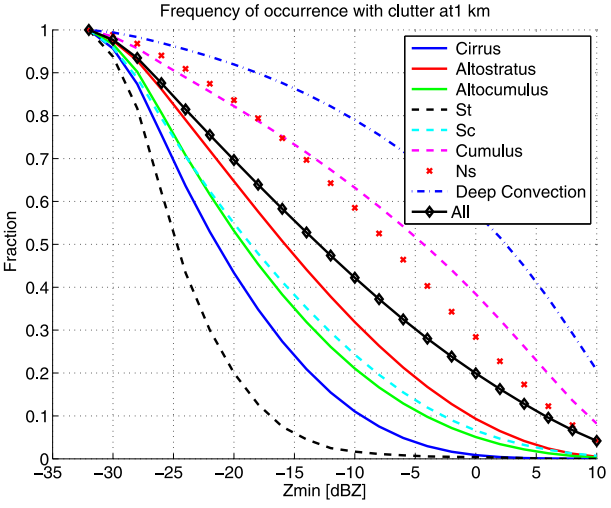


FIG. 15. Cloud detection as a function of a W-band minimum reflectivity for different cloud types as classified in the 2B-CLDCLASS (Mace et al. 2007). *CloudSat* is assumed as a reference (i.e., a detection level of 100% corresponds to detecting all clouds seen by *CloudSat*).

*Acknowledgments.* The portion of work carried out by Battaglia and Kollias was supported by the European Space Agency under the WISDR (Capability of Atmospheric Parameter Retrieval and Modeling for Wide-Swath Spaceborne Doppler Radars) activity (ITT AO/1-6661/11/NL/LvH) and by CEOI under the Polarization Diversity Doppler Radar on Satellite (POLYDOROS) project. The WRF simulation outputs have been kindly provided by Dr. S. Tanelli and Dr. A. Parodi. We thank Prof. E. Smith for his meticulous revision of the paper.

## REFERENCES

Amayenc, P., J. Testud, and M. Marzoug, 1993: Proposal for a spaceborne dual-beam rain radar with Doppler capability. *J. Atmos. Oceanic Technol.,* **10,** 262–276, doi:10.1175/1520-0426(1993)010<0262:PFASDB>2.0.CO;2.

Apel, J. R., 1994: An improved model of the ocean surface wave vector spectrum and its effects on radar backscatter. *J. Geophys. Res.,* **99,** 16 269–16 291, doi:10.1029/94JC00846.

Battaglia, A., and C. Simmer, 2008: How does multiple scattering affect the spaceborne W-band radar measurements at ranges close to and crossing the sea-surface range? *IEEE Trans. Geosci. Remote Sens.,* **46,** 1644–1651, doi:10.1109/TGRS.2008.916085.

——, and S. Tanelli, 2011: DOMUS: DOppler Multiple-Scattering Simulator. *IEEE Trans. Geosci. Remote Sens.,* **49,** 442–450, doi:10.1109/TGRS.2010.2052818.

——, and P. Kollias, 2014: Using ice clouds for mitigating the EarthCARE Doppler radar mispointing. *IEEE Trans. Geosci. Remote Sens.,* **53,** 2079–2085, doi:10.1109/TGRS.2014.2353219.

——, M. O. Ajewole, and C. Simmer, 2007: Evaluation of radar multiple scattering effects in CloudSat configuration. *Atmos. Chem. Phys.,* **7,** 1719–1730, doi:10.5194/acp-7-1719-2007.

——, J. M. Haynes, T. L'Ecuyer, and C. Simmer, 2008: Identifying multiple-scattering-affected profiles in CloudSat observations over the oceans. *J. Geophys. Res.,* **113,** D00A17, doi:10.1029/2008JD009960.

——, S. Tanelli, S. Kobayashi, D. Zrnić, R. Hogan, and C. Simmer, 2010: Multiple-scattering in radar systems: A review. *J. Quant. Spectrosc. Radiat. Transfer,* **111,** 917–947, doi:10.1016/j.jqsrt.2009.11.024.

——, T. Augustynek, S. Tanelli, and P. Kollias, 2011: Multiple scattering identification in spaceborne W-band radar measurements of deep convective cores. *J. Geophys. Res.,* **116,** D19201, doi:10.1029/2011JD016142.

——, S. Tanelli, and P. Kollias, 2013: Polarization diversity for millimeter spaceborne Doppler radars: An answer for observing deep convection? *J. Atmos. Oceanic Technol.,* **30,** 2768–2787, doi:10.1175/JTECH-D-13-00085.1.

——, ——, G. Heymsfield, and L. Tian, 2014: The dual wavelength ratio knee: A signature of multiple scattering in airborne Ku–Ka observations. *J. Appl. Meteor. Climatol.,* **53,** 1790–1808, doi:10.1175/JAMC-D-13-0341.1.

Bluestein, H. B., C. C. Weiss, and A. Pazmany, 2004: The vertical structure of a tornado near Happy, Texas, on 5 May 2002: High-resolution, mobile, W-band, Doppler radar observations. *Mon. Wea. Rev.,* **132,** 2325–2337, doi:10.1175/1520-0493(2004)132<2325:TVSOAT>2.0.CO;2.

——, and Coauthors, 2014: Radar in atmospheric sciences and related research: Current systems, emerging technology, and future needs. *Bull. Amer. Meteor. Soc.,* **95,** 1850–1861, doi:10.1175/BAMS-D-13-00079.1.

Doviak, R. J., and D. S. Zrnić, 1984: *Doppler Radar and Weather Observations.* Academic Press, 458 pp.

ESA, 2006: Earthcare mission requirements document. EarthCARE Mission Advisory Group Tech. Rep. EC-RS-ESA-Sy-012, Issue 5, 73 pp. [Available online at http://esamultimedia.esa.int/docs/EarthObservation/EarthCARE_MRD_v5.pdf.]

Eyre, J., J.-N. Thepaut, J. Joiner, L. P. Riishojgaard, and F. Gerard, 2002: Requirements for observations for global NWP. EUMETSAT Position Paper, 25 pp.

Gao, J., M. Xue, A. Shapiro, and K. K. Droegemeier, 1999: A variational method for the analysis of three-dimensional wind fields from two Doppler radars. *Mon. Wea. Rev.,* **127,** 2128–2142, doi:10.1175/1520-0493(1999)127<2128:AVMFTA>2.0.CO;2.

Guimond, S. R., L. Tian, G. M. Heymsfield, and S. J. Frasier, 2014: Wind retrieval algorithms for the IWRAP and HIWRAP airborne Doppler radars with applications to hurricanes. *J. Atmos. Oceanic Technol.,* **31,** 1189–1215, doi:10.1175/JTECH-D-13-00140.1.

Heymsfield, G. M., and Coauthors, 1996: The EDOP radar system on the high-altitude NASA ER-2 aircraft. *J. Atmos. Oceanic Technol.,* **13,** 795–809, doi:10.1175/1520-0426(1996)013<0795:TERSOT>2.0.CO;2.

——, J. B. Halverson, and I. J. Caylor, 1999: A wintertime Gulf Coast squall line observed by EDOP airborne Doppler radar. *Mon. Wea. Rev.,* **127,** 2928–2950, doi:10.1175/1520-0493(1999)127<2928:AWGCSL>2.0.CO;2.

——, ——, J. Simpson, L. Tian, and T. P. Bui, 2001: ER-2 Doppler radar investigations of the eyewall of Hurricane Bonnie during the Convection and Moisture Experiment-3. *J. Appl. Meteor.,* **40,** 1310–1330, doi:10.1175/1520-0450(2001)040<1310:EDRIOT>2.0.CO;2.

Hou, A. Y., and Coauthors, 2014: The Global Precipitation Measurement Mission. *Bull. Amer. Meteor. Soc.,* **95,** 701–722, doi:10.1175/BAMS-D-13-00164.1.

Illingworth, A. J., and Coauthors, 2015: The EarthCARE satellite: The next step forward in global measurements of clouds, aerosols, precipitation, and radiation. *Bull. Amer. Meteor. Soc.,* doi:10.1175/BAMS-D-12-00227.1, in press.

Joe, P., and Coauthors, 2010: The Polar Precipitation Measurement Mission. *Proc. Sixth European Conf. on Radar Meteorology and Hydrology,* Sibiu, Romania, EUMETSAT, 18 pp. [Available online at http://www.erad2010.org/pdf/oral/tuesday/satellite/01_ERAD2010_Joe.pdf.]

Kobayashi, S., H. Kumagai, and H. Kuroiwa, 2002: A proposal of pulse-pair Doppler operation on a spaceborne cloud-profiling radar in the W band. *J. Atmos. Oceanic Technol.,* **19,** 1294–1306, doi:10.1175/1520-0426(2002)019<1294:APOPPD>2.0.CO;2.

——, ——, and T. Iguchi, 2003: Accuracy evaluation of Doppler velocity on a spaceborne weather radar through a random signal simulation. *J. Atmos. Oceanic Technol.,* **20,** 944–949, doi:10.1175/1520-0426(2003)020<0944:AEODVO>2.0.CO;2.

Kollias, P., S. Tanelli, A. Battaglia, and A. Tatarevic, 2014: Evaluation of EarthCARE Cloud Profiling Radar Doppler velocity measurements in particle sedimentation regimes. *J. Atmos. Oceanic Technol.,* **31,** 366–386, doi:10.1175/JTECH-D-11-00202.1.

Kummerow, C. D., W. Barnes, T. Kozu, J. Shiue, and J. Simpson, 1998: The Tropical Rainfall Measuring Mission (TRMM) sensor package. *J. Atmos. Oceanic Technol.,* **15,** 809–817, doi:10.1175/1520-0426(1998)015<0809:TTRMMT>2.0.CO;2.

Mace, G. G., R. Marchand, Q. Zhang, and G. Stephens, 2007: Global hydrometeor occurrence as observed by CloudSat: Initial observations from summer 2006. *Geophys. Res. Lett.,* **34,** L09808, doi:10.1029/2006GL029017.

Matrosov, S., 2005: Attenuation-based estimates of rainfall rates aloft with vertically pointing Ka-band radars. *J. Atmos. Oceanic Technol.,* **22,** 43–54, doi:10.1175/JTECH-1677.1.

Meneghini, R., and T. Kozu, 1990: *Spaceborne Weather Radar.* Artech House Radar Library, Artech House, 199 pp.

Mitrescu, C., T. L. Ecuyer, J. Haynes, S. Miller, and J. Turk, 2010: *CloudSat* precipitation profiling algorithm—Model description. *J. Appl. Meteor. Climatol.,* **49,** 991–1003, doi:10.1175/2009JAMC2181.1.

Pazmany, A., J. Galloway, J. Mead, I. Popstefanija, R. McIntosh, and H. Bluestein, 1999: Polarization diversity pulse-pair technique for millimeter-wave Doppler Radar measurements of severe storm features. *J. Atmos. Oceanic Technol.,* **16,** 1900–1910, doi:10.1175/1520-0426(1999)016<1900:PDPPTF>2.0.CO;2.

Romeiser, R., W. Alpers, and V. Wismann, 1997: An improved composite surface model for the radar backscattering cross section of the ocean surface: 1. Theory of the model and optimization/validation by scatterometer data. *J. Geophys. Res.,* **102,** 25 237–25 250, doi:10.1029/97JC00190.

Schutgens, N. A. J., 2008: Simulated Doppler radar observations of inhomogeneous clouds: Application to the EarthCARE space mission. *J. Atmos. Oceanic Technol.,* **25,** 1514–1528, doi:10.1175/2007JTECHA1026.1.

Simpson, J., C. Kummerow, W.-K. Tao, and R. Adler, 1996: On the Tropical Rainfall Measuring Mission (TRMM). *Meteor. Atmos. Phys.,* **60,** 19–36, doi:10.1007/BF01029783.

Skamarock, W. C., and J. B. Klemp, 2008: A time-split nonhydrostatic atmospheric model for research and NWP applications. *J. Comput. Phys.,* **227,** 3465–3485, doi:10.1016/j.jcp.2007.01.037.

——, ——, J. Dudhia, D. O. Gill, D. M. Barker, W. Wang, and J. G. Powers, 2005: A description of the advanced research WRF version 2. NCAR Tech Note NCAR/TN-468+STR, 88 pp. [Available online at http://www.mmm.ucar.edu/wrf/users/docs/arw_v2.pdf.]

Smith, E. A., and Coauthors, 2007: International Global Precipitation Measurement (GPM) program and mission: An overview. *Measuring Precipitation from Space: EURAINSAT and the Future,* V. Levizzani, P. Bauer, and F. J. Turk, Eds., Advances in Global Change Research, Vol. 28, Springer, 611–653.

Snyder, C., and F. Zhang, 2003: Assimilation of simulated Doppler radar observations with an ensemble Kalman filter. *Mon. Wea. Rev.,* **131,** 1663–1677, doi:10.1175//2555.1.

Stephens, G. L., and Coauthors, 2002: The CloudSat mission and the A-Train. *Bull. Amer. Meteor. Soc.,* **83,** 1771–1790, doi:10.1175/BAMS-83-12-1771.

——, and Coauthors, 2008: CloudSat mission: Performance and early science after the first year of operation. *J. Geophys. Res.,* **113,** D00A18, doi:10.1029/2008JD009982.

Stoffelen, A., M. Bonavita, J. Eyre, M. Goldberg, H. Jarvinen, C. Serio, J.-N. Thepaut, and V. Wulfmeyer, 2006: Post-EPS developments on atmospheric sounding and wind profiling. EUMETSAT Position Paper, 36 pp.

Sy, O., S. Tanelli, N. Takahashi, Y. Ohno, H. Horie, and P. Kollias, 2013: Simulation of EarthCARE spaceborne Doppler radar products using ground-based and airborne data: Effects of aliasing and non-uniform beam-filling. *IEEE Trans. Geosci. Remote Sens.,* **52,** 1463–1479, doi:10.1109/TGRS.2013.2251639.

——, ——, P. Kollias, and Y. Ohno, 2014: Application of matched statistical filters for EarthCARE cloud Doppler products. *IEEE Trans. Geosci. Remote Sens.,* **52,** 7297–7316, doi:10.1109/TGRS.2014.2311031.

Tanelli, S., E. Im, S. L. Durden, L. Facheris, and D. Giuli, 2002: The effects of nonuniform beam filling on vertical rainfall velocity measurements with a spaceborne Doppler radar. *J. Atmos. Oceanic Technol.,* **19,** 1019–1034, doi:10.1175/1520-0426(2002)019<1019:TEONBF>2.0.CO;2.

——, ——, ——, ——, ——, and E. Smith, 2004: Rainfall Doppler velocity measurements from spaceborne radar: Overcoming nonuniform beam-filling effects. *J. Atmos. Oceanic Technol.,* **21,** 27–44, doi:10.1175/1520-0426(2004)021<0027:RDVMFS>2.0.CO;2.

——, S. Durden, E. Im, K. Pak, D. Reinke, P. Partain, J. Haynes, and R. Marchand, 2008: CloudSat's Cloud Profiling Radar after 2 years in orbit: Performance, calibration, and processing. *IEEE Trans. Geosci. Remote Sens.,* **46,** 3560–3573, doi:10.1109/TGRS.2008.2002030.

——, G. M. Heymsfield, G. S. Stephens, S. L. Durden, E. Im, P. Racette, L. Li, and G. Sadowy, 2010: Decadal survey tier 2 mission study summative progress report: ACE radar. JPL/NASA Doc., 14 pp. [Available online at http://hdl.handle.net/2014/41978.]

Testud, J., and P. Amayenc, 1989: Stereoradar meteorology: A promising technique for observation of precipitation from a mobile platform. *J. Atmos. Oceanic Technol.,* **6,** 89–108, doi:10.1175/1520-0426(1989)006<0089:SMAPTF>2.0.CO;2.

——, ——, and M. Marzoug, 1992: Rainfall-rate retrieval from a spaceborne radar: Comparison between single-frequency, dual-frequency, and dual-beam techniques. *J. Atmos. Oceanic Technol.,* **9,** 599–623, doi:10.1175/1520-0426(1992)009<0599:RRRFAS>2.0.CO;2.

Ulaby, F. T., R. K. Moore, and A. K. Fung, 1986: *Microwave Remote Sensing Fundamental and Radiometry.* Vol. 1, *Microwave Remote Sensing: Active and Passive,* Artech House, 456 pp.

Yuter, S. E., and R. A. Houze, 1995: Three-dimensional kinematic and microphysical evolution of Florida cumulonimbus. Part II: Frequency distributions of vertical velocity, reflectivity, and differential reflectivity. *Mon. Wea. Rev.,* **123,** 1941–1963, doi:10.1175/1520-0493(1995)123<1941:TDKAME>2.0.CO;2.

Zhang, F., Y. Weng, J. A. Sippel, Z. Meng, and C. H. Bishop, 2009: Cloud-resolving hurricane initialization and prediction through assimilation of Doppler radar observations with an ensemble Kalman filter. *Mon. Wea. Rev.,* **137,** 2105–2125, doi:10.1175/2009MWR2645.1.

Zrnić, D. S., 1977: Spectral moment estimates from correlated pulse pairs. *IEEE Trans. Aerosp. Electron. Syst.,* **AES-13,** 344–354, doi:10.1109/TAES.1977.308467.